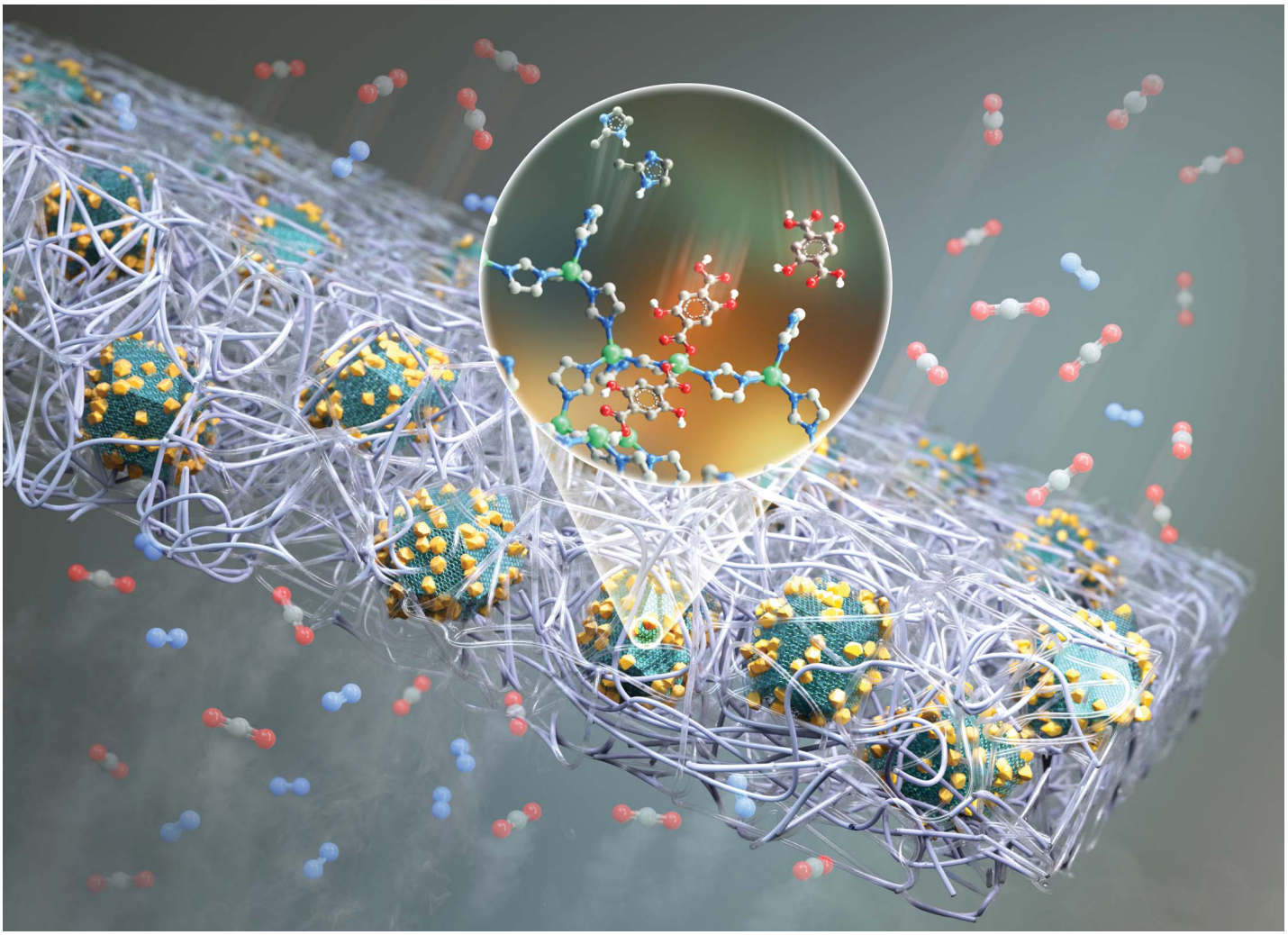

Showcasing research from Professor Won Seok Chi's laboratory, School of Polymer Science and Engineering, Chonnam National University, Gwangju, Republic of Korea.

Decorating Zn-MOF-74 on ZIF-8 to increase gas transport and plasticization resistance in mixed-matrix membranes

Zn-MOF-74 was decorated on ZIF-8 nanoparticles *via* a ligand exchange method. The open metal sites of Zn-MOF-74 increased CO_2 sorption and compatibility with the carboxylated polymer matrix. The Zn-MOF-74 decorated ZIF-8 mixed-matrix membrane showed an improvement in gas separation performance and CO_2 plasticization resistance.

Image reproduced by permission of Won Seok Chi from *J. Mater. Chem. A*, 2026, **14**, 17846.

As featured in:

See Dongkyu Roh, Won Seok Chi *et al.*, *J. Mater. Chem. A*, 2026, **14**, 17846.

ROYAL SOCIETY OF CHEMISTRY

rsc.li/materials-a

Registered charity number: 207890

Journal of Materials Chemistry A

ROYAL SOCIETY OF CHEMISTRY

PAPER

View Article Online
View Journal | View Issue

Cite this: J. Mater. Chem. A, 2026, 14, 17846

Decorating Zn-MOF-74 on ZIF-8 to increase gas transport and plasticization resistance in mixed-matrix membranes

Jin Hui Jo,[a] Jieun Lee,[a] Eun Ji An,[a] Hyomin Choi,[a] Hyunmo Jae,[bc] Yubin Lee,[d] Miso Kang,[d] Jaesung Park,[d] Hyuk Taek Kwon,[e] Chanmin Lee,[fg] Dongkyu Roh *[c] and Won Seok Chi *[ah]

Received 22nd September 2025
Accepted 28th March 2026

DOI: 10.1039/d5ta07747h

rsc.li/materials-a

The rational interfacial design of MOF-polymer mixed-matrix membranes (MMMs) is essential for achieving both high gas-separation performance and long-term stability. Conventional functional group-tethering methods improve MOF-polymer compatibility but involve complex synthesis and are difficult to generalize. Herein, we report a facile ligand-exchange strategy to decorate ZIF-8 nanoparticles with Zn-MOF-74 using 2,5-dihydroxyterephthalic acid (DHTA), creating nanoparticles with hydroxyl-rich ligand groups and open metal sites inherent to the Zn-MOF-74 characteristics that form strong interactions with the 6FDD polyimide matrix. This interfacial engineering not only enhances the mechanical and physicochemical stability of the MMM but also increases pore window size and gas sorption sites. As a result, the series of 20 wt% Zn-MOF-74@ZIF-8/6FDD MMMs exhibit greatly improved gas permeabilities (H_2: 627 Barrer; CO_2: 463 Barrer) compared to pristine 6FDD membranes (H_2: 106 Barrer; CO_2: 116 Barrer) while maintaining excellent high-pressure CO_2 plasticization resistance.

Introduction

Gas-separation membranes have attracted attention due to their high energy efficiency, environmental friendliness, compact module size, and small footprint.[1,2] In particular, their low energy consumption based on concentration difference-driven transport without thermally-driven phase transition (*e.g.*, liquid phase to gas phase) for membrane-based separation makes them suitable for replacing traditional separation units involving distillation or absorption.[3] Commercially available polymer materials for membrane fabrication with excellent attributes, such as excellent processability and low cost, can be used to form large-scale spiral wound-type or hollow fiber-type membranes.[1–4] However, the resulting polymer membranes have notorious drawbacks, such as (1) the permeability-selectivity trade-off relationship defined by the upper-bound limit and (2) plasticization caused by highly soluble gases under a high feed pressure.[5–7] These phenomena limit the separation performance or cause low membrane stability, which has hampered their commercial applicability in industry.

Many researchers have incorporated metal–organic framework (MOF) nanoparticles into the polymer matrix to form mixed-matrix membranes (MMMs), thereby increasing molecular transport *via* porous media and preventing the polymer chains from swelling due to plasticization.[8–11] MOFs are highly porous crystalline materials composed of metal ions (or clusters) and organic linkers. They exhibit very high porosity, a tuneable pore aperture, controllable external/internal architecture, and high chemical/thermal stability, among other attributes.[12] Their unique characteristics can be tailored by selective component combination, thereby enabling their usage in applications such as separation, catalysis, and chemical/biological sensing.[13–16]

Zeolitic imidazolate frameworks (ZIFs), a subclass of MOFs, have recently received remarkable attention for gas separation due to their well-defined porous structure (theoretical pore size: 3.4 Å and effective pore size: 4.4 Å).[17–20] Of practical importance, ZIF-8 can be formed into nano-sized particles at room temperature after a short reaction time.[21,22] However, ZIF-8 lacks

[a]Department of Polymer Engineering, Graduate School, Chonnam National University, 77 Yongbong-ro, Bukgu, Gwangju 61186, Republic of Korea
[b]Department of Chemical and Biochemical Engineering, Yonsei University, 50 Yonsei-ro, Seodaemun-gu, Seoul 03722, Republic of Korea
[c]Energy & Environment Division, Korea Institute of Ceramic Engineering and Technology (KICET), 101, Soho-ro, Jinju-si, Gyeongsangnam-do 52851, Republic of Korea. E-mail: rohdk@kicet.re.kr
[d]Chemical & Process Technology Division, Korea Research Institute of Chemical Technology (KRICT), 141, Gajeongro, Yuseong, Daejeon 34114, Republic of Korea
[e]Department of Chemical Engineering, Pukyoung National University, 45 Youngso-ro, Nam-gu, Busan 48513, Republic of Korea
[f]Green Circulation R&D Department, Research Institute of Sustainable Development Technology, Korea Institute of Industrial Technology, 89 Yangdaegiro-gil, Ipjan-myeon, Seobuk-gu, Cheonan-si 31056, Chungcheongnam-do, Republic of Korea
[g]Department of Chemical Engineering, Chung-Ang University, 84 Heokseok-ro, Dongjak-gu, Seoul 31056, Republic of Korea
[h]School of Polymer Science and Engineering, Chonnam National University, 77 Yongbong-ro, Buk-gu, Gwangju 61186, Republic of Korea. E-mail: wschi@jnu.ac.kr

organic functional groups that can interact with a polymer matrix, leading to defect formation at the MOF-polymer interface that compromises the membrane performance. To address this issue, researchers have introduced post-synthetic interfacial engineering approaches to organically functionalize the surface of MOF nanoparticles, thereby improving MOF-polymer interfacial compatibility.[23–26]

Another type of MOF, M-MOF-74 (M = Mg, Mn, Co, Fe, Ni, or Zn, among others), can be formed *via* the coordination between the metal ion and organic ligand 2,5-dihydroxyterephthalic acid (DHTA). DHTA was deliberately selected in this study because it not only dictates the formation of the MOF-74 topology but also introduces coordination sites that generate open metal sites and promote strong interfacial interactions with functional polymers. Notable features of M-MOF-74 include a high density of unsaturated metal sites and a large pore size of approximately 11 Å, which make it particularly suitable for the separation of highly soluble gases such as CO_2 or hydrocarbons.[27–29] While an increase in effective pore size typically enhances gas permeability, excessive enlargement can decrease the kinetic size-sieving effects and reduce selectivity when the pore aperture approaches or exceeds the kinetic diameters of the target gas molecules. Nevertheless, rational pore enlargement or the introduction of hierarchical porosity can enhance overall gas transport without necessarily sacrificing, and in some cases even improving diffusive selectivity, provided that the resulting pore size distribution and connectivity remain within a regime where one component experiences stronger confinement or faster diffusion than its competitor.[30] However, synthesizing M-MOF-74 into externally well-defined nano-sized crystals with a large surface area remains significantly challenging. Several approaches to form M-MOF-74 particles have been reported, such as the microwave heating method,[31–33] the multi-step solvothermal method,[34] and the agent-assisted synthetic method.[35,36] However, these synthetic routes either provide a large particle size (likely micron-sized), a relatively reduced crystalline structure, or a low BET surface area, which are not sufficient for the MOF filler in MMMs for efficient gas separation.

Since pure MOFs, ZIF-8 and M-MOF-74 each have specific drawbacks, it is difficult to achieve ideal MOF-polymer interfacial compatibility and exceptional gas transport properties when they are incorporated into a polymer matrix. Thus, we can employ an alternative MOF integration approach to provide the ideal MOF filler in MMMs by constructing MOF-on-MOF hybrid structures.[31,34,37] The MOF-on-MOF approach not only enhances the structural stability and chemical versatility of the resulting material but also enables the development of unique properties while simultaneously overcoming the inherent drawbacks of using a single MOF.[38–42] Moreover, synergistic interactions between the appropriately selected different MOFs can improve molecular transport and compatibility with the polymer matrix by overcoming the limitations of conventional MOFs.[43–48]

Conventional approaches to improving MOF-polymer interfacial compatibility in MMMs typically involve MOF surface functionalization,[49–53] modification of the polymer matrix,[54–56] using coupling agents,[24,57–59] or ionic liquids[60–62] as interfacial modifiers. Although these strategies can effectively reduce interfacial voids, they often require additional synthetic steps, are highly system-specific, and may partially block MOF pores. In this context, MOF-on-MOF architectures have been explored as an alternative filler design strategy in MMMs, aiming to combine distinct MOF functionalities within a single particle rather than relying on extensive surface or matrix modification. Most previously reported MOF-on-MOF fillers for gas separation MMMs employ ZIF-8 as an external shell on a hydrophilic or water-sensitive core (*e.g.*, MIL-101(Cr)@ZIF-8, HKUST-1@ZIF-8, NH_2-MIL-125@ZIF-8, ZIF-67@ZIF-8, UiO-66@ZIF-8, ZIF-11@ZIF-8 and NH_2-MIL-53@ZIF-8), where ZIF-8 mainly functions as a hydrophobic or molecular-sieving layer and the core serves as a high-porosity reservoir.[44,63–69] In this work, we invert both the architecture and functional roles by designing a ZIF-8@MOF-74 system in which Zn-MOF-74, with one-dimensional channels and abundant open metal sites, forms directly contacting the polymer matrix, while ZIF-8 constitutes the inner core providing rigidity and good dispersion at high loadings. Such a Zn-MOF-74 formation on ZIF-8 filler has not been previously explored for MMMs, offering a distinct route to enhance both permeability and selectivity *via* interfacial and hierarchical pore engineering.

Herein, we present the chemical engineering of a novel MOF-on-MOF structure composed of ZIF-8 and Zn-MOF-74 nanoparticles containing the same metal ion (Zn) for the rational design of effective MMMs to achieve efficient gas separation. This hybrid structure was developed by partially growing Zn-MOF-74 on already synthesized ZIF-8 nanoparticles using a post-modification ligand-exchange method. The Zn-MOF-74 conversion ratio was systematically engineered based on the ligand concentration for the exchange process that partially grew over the readily synthesized ZIF-8 nanoparticles.

The resulting MOF nanoparticles combine the high yield and structural robustness of ZIF-8 with the larger pore channels and accessible metal sites characteristic of Zn-MOF-74, thereby exhibiting hybrid features that are not attainable using ZIF-8 nanoparticles alone. The 4,4′-(hexafluoroisopropylidene)diphthalic anhydride (4,4′-(hexafluoroisopropylidene)diphthalic anhydride (6FDA)-DAM (2,4,6-trimethyl-1,3-diaminobenzene) : 3,5-diamino-benzoic acid (DABA) (3 : 2), 6FDD) was chosen for the polymer matrix to fabricate MMMs with Zn-MOF-74 decorated ZIF-8 nanoparticles. 6FDD polyimide is a conventional aromatic polyimide incorporating carboxylic acid functionalities, which has been widely reported to be readily synthesized and suitable for membrane fabrication.[70] In particular, the coordination interactions and hydrogen bonding between the carboxylate groups in 6FDD polyimide and Zn-MOF-74 (with hydroxyl ligands and open metal sites) are expected to enhance the MOF-polymer compatibility. This strengthened interfacial adhesion suppresses non-selective interfacial voids and restricts polymer chain swelling, thereby promoting the controlled MOF-dominated gas transport.[71–75]

We also investigated the material characteristics, gas-separation performance, and high-pressure carbon dioxide (CO_2) gas plasticization behaviour of subsequently fabricated Zn-MOF-74-decorated ZIF-8 based MMMs with a systematically tunable Zn-MOF-74 conversion ratio and variable MOF weight loading.

Experimental section

Materials

Zinc nitrate hexahydrate ($Zn(NO_3)_2 \cdot 6H_2O$, 98%) and 2-methylimidazole (2MeIM, 99%) were purchased from Sigma-Aldrich (St. Louis, MO, USA). DHTA was purchased from Tokyo Chemical Industry (Tokyo, Japan). Tetrahydrofuran (THF, 99.0%) was purchased from Daejung Chemicals (Siheung, Republic of Korea). Methanol (MeOH) was purchased from Duksan Chemicals (Ansan, Republic of Korea). 6FDD (M_w = 210 kDa, polydispersity index = 2.5) was purchased from Akron Polymer Systems. All chemicals were used as received without further purification. Gas cylinders containing hydrogen (H_2), nitrogen (N_2), methane (CH_4), or carbon dioxide (CO_2) gas of ultra-high purity grade (>99.999%) were purchased from Hankook Multiple Gas (Bucheon, Republic of Korea).

Synthesis of ZIF-8 nanoparticles

This was performed using the following procedure.[76] 2MeIM (6.6 g) and $Zn(NO_3)_2 \cdot 6H_2O$ (3.3 g) were separately dissolved in 200 mL of MeOH (200 mL) each. Once both solutions became clear, the $Zn(NO_3)_2$ solution was poured into the ligand solution while stirring. The solutions were combined and vigorously stirred for 1 hour at room temperature, followed by centrifugation. The resulting white nanoparticles were thoroughly washed three times with MeOH. The final product was dried in an oven at 60 °C overnight, followed by further drying in a vacuum oven at 60 °C overnight.

Decoration of the ZIF-8 nanoparticles with Zn-MOF-74

This was accomplished *via* a ligand-exchange method by slightly modifying a previously reported one.[77] Briefly, the synthesized ZIF-8 nanoparticles (0.3 g) were initially dispersed in MeOH (200 mL). Meanwhile, three DHTA solutions were prepared by dissolving 0.016, 0.025, or 0.05 g DHTA in MeOH (200 mL) to form Zn-MOF-74-decorated ZIF-8 nanoparticles (ZIF-8@MOF-74) with a ZIF-8 : DHTA concentration ratio of 18 : 1, 12 : 1, or 6 : 1, respectively. To this end, one of the DHTA solutions was added to the ZIF-8 nanoparticle dispersion solution, after which the mixture solution was stirred for 20 min at room temperature, followed by aging for 30 min at room temperature. To eliminate unreacted species and impurities, the resulting products were thoroughly washed with fresh MeOH solvent for short intervals and centrifuged at 12 000 rpm, which was repeated several times. The obtained yellowish powders were dried in an oven and a vacuum oven at 60 °C overnight, each. Hereafter, ZIF-8@MOF-74 with ZIF-8 : DHTA concentration ratios of 18 : 1, 12 : 1, and 6 : 1 are denoted as ZIF-8@MOF-74-1, ZIF-8@MOF-74-2, and ZIF-8@MOF-74-3, respectively.

Fabrication of a pure 6FDD and ZIF-8@MOF-74 MMMs

These were fabricated using a solution-casting and solvent-evaporation method. For the pure 6FDD polyimide membrane, 6FDD polyimide (0.15 g) was dissolved in THF solvent (6 mL). The homogeneous polymer solution was poured into a glass Petri dish and then covered with aluminum foil through which a few small holes had been made to maintain a slow evaporation rate. The solvent was completely evaporated in an oven at 50 °C overnight, resulting in a self-standing 6FDD polyimide membrane. The membrane was detached from the glass Petri dish and dried in a vacuum oven at 60 °C to completely remove any residual solvent. For the ZIF-8-containing MMMs, 6FDD polyimide and ZIF-8 (or ZIF-8@MOF-74) nanoparticles (the total weight of 6FDD and MOF was set as 0.15 g) were dissolved (or dispersed) in THF solvent (6 mL). Of note, the MOF weight loadings were set as 0, 10, and 20 wt%. The weight loading values of MOFs in the MMM were calculated using the following equation:

$$\text{MOF weight loading(wt\%)} = \frac{\text{MOF(g)}}{\text{polymer(g)} + \text{MOF(g)}} \times 100\% \quad (1)$$

For the priming method, the MOF and 6FDD solutions were prepared separately. To uniformly disperse the MOF nanoparticles in the THF solvent, the MOF solution was vigorously stirred using a magnetic stirrer bar for 2 h and then bath-sonicated for 30 min. Once the 6FDD polyimide solution was added to the MOF solution, the mixture solution was stirred for a few hours to ensure uniform MOF distribution in the 6FDD polyimide matrix. The solution-casting, solvent-evaporation, membrane-formation, and drying processes were then conducted as previously described for the 6FDD polyimide membrane fabrication method.

Gas permeation test

A custom-built, automated variable-pressure, constant-volume setup with permeation system (NFEC-2025-02-303251) was used to conduct single-gas permeation tests for H_2, N_2, CH_4, and CO_2 at 35 °C and 15 psi. Before measuring the gas permeation performance, the membranes were dried overnight in a vacuum oven at 60 °C to completely remove any residual solvent trapped in the polymer chains or MOF pores. A custom-made brass disk with a small activated hole in the center was fabricated. The membrane was cut to match the size of the activation hole, and its thickness was measured multiple times using a micrometer to determine the average thickness. Epoxy (5 minute Devcon) was applied to seal any defects between the membrane and the brass disk hole. The active area was then determined from an image of the membrane obtained using a scanner and processed using ImageJ software before being placed into the permeation cell. The latter was maintained at 35 °C using an air-circulating heater. Before testing, the sample was kept under dynamic vacuum conditions for at least 6 h to remove any residual solvent and activate the open metal sites of the MOF nanoparticles. Leak testing was performed prior to the experiment to determine the precise gas transport rate by subtracting the leak rate from the total gas transport rate under static vacuum conditions. For the single-gas permeation tests, H_2, N_2, CH_4, and CO_2 gas was gradually injected at 15 psi. The

gas transport rate was measured at least 6–10 times for the time lag to ensure a steady state. High-pressure CO_2 plasticization testing was conducted to evaluate the stability of the membrane under harsh conditions. To ensure steady-state conditions, CO_2 gas was injected at pressures ranging from 15 to 750 psi in increments of 75 psi from the upstream to the downstream side with equal holding times. CO_2 permeability at all feed pressure points was calculated and normalized based on the permeability at 15 psi.

Characterization

Fourier transform infrared (FT-IR) spectroscopy using a Spectrum 100 FT-IR spectrometer (PerkinElmer, USA), with 32 scans at a resolution of 4 cm^{-1} in the wavenumber range from 4000 to 350 cm^{-1}, was performed to investigate the chemical structures of the compounds. The crystalline structures of the MOF nanoparticles and corresponding MOF MMMs were elucidated by using X-ray diffraction (XRD) analysis *via* a D/MAX Ultima III diffractometer (Rigaku, Japan) at a scan rate of 3° min^{-1} from 5 to 50°. The N_2 adsorption–desorption isotherms, BET surface areas, and pore size distributions were obtained *via* BET analysis using a Belsorp-MAX instrument (Belsorp, Japan) at 77 K. The H_2, N_2, CH_4, and CO_2 single gas adsorption isotherms at 308.15 K were obtained by Microtrac BEL (BELSORP MAX II). The MOF powders were prepared *via* degassing using a Belprep-VAC II vacuum degasser (MicrotracBEL, Japan) at 150 °C for 6 h. Field-emission (FE)-scanning electron microscopy (SEM) was conducted using a JSM-7610F instrument (JEOL, Japan) to examine the morphology and size of MOF nanoparticles and to obtain cross-sectional images of the membranes. Corrected scanning-transmission electron microscopy (TEM) was performed with a TF30ST instrument (FEI, USA) equipped with an energy dispersive X-ray spectrometer to analyze the internal and external morphology of MOF nanoparticles and perform elemental distribution mapping across these areas, respectively. To prepare the samples for TEM analysis, a 0.5 wt% MOF dispersion in methanol was prepared and cast onto a copper grid. To investigate the morphology of the ZIF-8@MOF-74 nanoparticles, aberration-corrected scanning transmission electron microscopy (STEM) was performed using a JEM-ARM300F instrument (JEOL Ltd, Japan) operated at 160 kV and equipped with a Gatan electron energy-loss spectrometer (EELS). EELS analyses were conducted to examine the core-loss edges of selected elements across the designated regions. The acquired spectra were processed using Gatan Digital Micrograph software. X-ray photoelectron spectroscopy (XPS) was performed using a VersaProbe instrument (ULVAC-PHI, Japan) to analyze the elemental composition and chemical bonds of the MOF nanoparticles. The thermal stability and actual MOF loadings in the MMMs were evaluated *via* thermogravimetric analysis (TGA) using a TGA2 instrument (Mettler Toledo, Switzerland) over a temperature range of 35 to 700 °C under an air atmosphere. The mechanical properties of the membranes were assessed *via* a universal testing machine (UTM) (MCT-2150, Japan) at a stretching rate of 2.5 mm min^{-1}. Dissolution testing was conducted to assess the stability and interactions between the MOF and the polymer. To compare the stability of a membrane, its weight was measured before and after immersion in THF (a solvent known to effectively dissolve 6FDD polyimide). To elucidate the chemical stability of the MMMs, the glass transition temperature (T_g) was determined using a DSC3 instrument (Mettler Toledo, Switzerland). Measurements were conducted over a temperature range of 25 to 450 °C at a heating rate of 10 K min^{-1} under a nitrogen atmosphere. To eliminate T_g effectively, a second heating scan was performed after the first heating and cooling cycle over the same temperature range, and the apparent T_g was determined from the second heating run.

Results and discussion

Synthesis and characterization of ZIF-8 nanoparticles and ZIF-8@MOF-74

We synthesized ZIF-8 nanoparticles with and without decorating them with Zn-MOF-74. The ZIF-8 nanoparticles exhibited a sodalite topology while Zn-MOF-74 presented a honeycomb topology (Fig. S1). The theoretical pore sizes of the ZIF-8 nanoparticles and Zn-MOF-74 were approximately 3.4 and 11 Å, respectively. Initially, Zn-MOF-74 showed micron-sized particles (Fig. S2), thereby illustrating the challenge of synthesizing well-defined nano-sized particles of this material. Thus, we employed ligand-exchanged post-modification of ZIF-8 nanoparticles based on the same metal ion to decorate the ZIF-8 nanoparticle surfaces with Zn-MOF-74. Subsequently, ZIF-8@MOF-74 nanoparticles were synthesized by post-modifying ZIF-8 nanoparticles *via* a ligand-exchange method from 2MeIM to DHTA, as shown in Scheme 1.

Given the inherent characteristics of MOFs, ZIF-8 nanoparticles were formed *via* coordination bonds between the Zn ions and the 2MeIM organic ligand. The formation of a Zn-MOF-74 *via* the ligand-exchange method on ZIF-8 particles is thermodynamically driven by differences in coordination stability and ligand acidity. In ZIF-8, Zn^{2+} centers are coordinated by monodentate imidazolate ligands (Zn–N bonds), which exhibit a relatively modest stability constant ($\log K \sim 2.5$).[78] In contrast, coordination of Zn^{2+} with DHTA proceeds *via* a bidentate chelating mode, forming Zn-dicarboxylate complexes with a substantially higher overall stability constant ($\log \beta_2 \sim 8$), reflecting the thermodynamic stabilization associated with the chelate effect.[78] In particular, DHTA demonstrates a notably heightened coordination ability

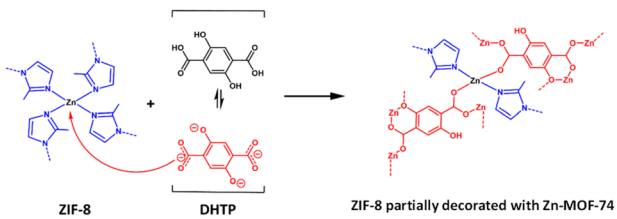

Scheme 1 A schematic illustration of Zn-MOF-74-decorated ZIF-8 nanoparticle synthesis *via* a ligand-exchange method.

compared to 2MeIM, thereby facilitating a more pronounced and effective ligand-exchange process.[77] This feature enabled the ZIF-8 nanoparticles to be converted to Zn-MOF-74 nanoparticles based on coordination between the same Zn ion being present in both *via* dynamic ligand exchange between 2MeIM and DHTA on the surface of the ZIF-8 nanoparticles. This ligand exchange is further facilitated by the pronounced difference in acidity between the two ligands. DHTA ($pK_a \sim 2.17$)[79] is more acidic than the 2MeIM ($pK_a \sim 7.85$),[80] which promotes preferential deprotonation of DHTA under solvothermal conditions and formation of strongly coordinating carboxylate anions ($R–COO^-$). Consequently, Zn-DHTA coordination becomes thermodynamically favoured over Zn-imidazolate bonding at the particle surface. Dissolved DHTA exhibits weak acidic properties in MeOH solution, leading to the formation of $DHTA^{4-}$. The $DHTA^{4-}$ etches the surface of the ZIF-8 nanoparticles, leading to the exposure of Zn^{2+} that serves as nucleation sites for subsequent coordination and surface growth of Zn-MOF-74.[81] Collectively, the combined effects of enhanced chelate stability and stronger ligand acidity promote partial interfacial reconstruction of ZIF-8, leading to the development of a Zn-MOF-74.

Fig. 1a and b depict FT-IR spectra and XRD patterns for ZIF-8 and ZIF-8@MOF-74 nanoparticles, respectively. The FT-IR spectra for the ZIF-8 nanoparticles in Fig. 1a shows an absorption band at 420 cm^{-1} due to the presence of Zn–N coordination bonds, thus confirming that the coordination process between the Zn ions and the 2MeIM organic ligand had taken place (Fig. S3a).[23,68,82] In addition, the FT-IR spectrum for the ZIF-8 nanoparticles in Fig. 1a exhibits noticeable peaks at 1311 and 1146 cm^{-1} corresponding to C–H and aromatic C–N vibrations in the imidazole ring, respectively.[23,68,83,84] The XRD pattern for ZIF-8 in Fig. 1b exhibits distinct diffraction peaks at $2\theta = 18.0$, 12.7, 10.4, and 7.3, corresponding to the (222), (211), (220), and (110) planes.[23,68,82] This result indicates that the ZIF-8 nanoparticles were highly crystalline, which is adaptable for the ligand-exchange approach to forming crystalline ZIF-8@MOF-74 nanoparticles.

The FT-IR spectrum for the ZIF-8@MOF-74 nanoparticles in Fig. 1a exhibits absorption bands at 1243 and 1196 cm^{-1} assigned to C–O stretching vibrations and $–COO^-$ asymmetric stretching vibrations in the exchanged DHTA ligand. In addition, notable peaks at 884 and 817 cm^{-1} correspond to the C–O–Zn group in the Zn-MOF-74.[85–88] The appearance of these new peaks reveals that the 2MeIM organic ligand was successfully exchanged with the DHTA organic ligand. Moreover, the peak intensities at 1145 and 1131 cm^{-1} (the C–N bond in the imidazole ring), and 420 cm^{-1} (the Zn–N bond) decreased, which is related to reduced coordination of the Zn–2MeIM bonds by increasing the Zn-MOF-74 conversion ratio.[9,23,76] The broad absorption bands at 3500 cm^{-1} corresponding to the –OH group in Fig. S3b indicate the successful incorporation of the DHTA ligand.

Fig. 1b presents XRD patterns for the ZIF-8, Zn-MOF-74, and ZIF-8@MOF-74 nanoparticles. The crystalline peaks in the pattern for the ZIF-8@MOF-74 nanoparticles appeared at similar 2θ locations to those in the pattern for ZIF-8 (from 5 to 25°), which indicates the presence of ZIF-8 nanoparticles in both materials. In particular, new peaks in the XRD patterns for the ZIF-8@MOF-74-2 and ZIF-8@MOF-74-3 nanoparticles appearing at 11.8 and 6.8° and corresponding to the (300) and (110) crystal planes, respectively, were not present in the pattern for the ZIF-8 nanoparticles.[89–91] This result reveals that the crystalline structure of the MOF nanoparticles was maintained after the ligand-exchange process. In addition, distinct crystalline peaks were present due to the partial crystalline phase transformation from ZIF-8 to Zn-MOF-74. Increasing the DHTA organic ligand concentration noticeably reduced the crystalline peak intensity compared to that in the XRD pattern for the ZIF-8 nanoparticles, which indicates that Zn-MOF-74 conversion was increased by enhancing the ligand-exchange facilitation.[89,90] Of particular interest, the diffraction peak at $2\theta = 7.34°$ in the pattern for the ZIF-8 nanoparticles was slightly shifted to a higher 2θ value with an increase in the Zn-MOF-74 conversion ratio; this is likely because of the lattice size of Zn-MOF-74 ($a =$ 6.7 Å and $b = c = 15.3$ Å) is smaller than that of ZIF-8 ($a = 17.08$ Å, $b = 17.06$ Å and $c = 17.04$ Å).[90,92–94]

The thermal stability of the ZIF-8 and ZIF-8@MOF-74 nanoparticles was examined using TGA under an air atmosphere. Interpreting the TGA profiles in Fig. 2a, the initial weight loss below 100 °C was due to the evaporation of residual solvent or water molecules trapped in the pores of the MOF structure. In particular, the TGA curve for ZIF-8@MOF-74 shows a higher weight loss in this temperature range, even after vacuum drying before the TGA was conducted, which is likely due to the open metal sites of Zn-MOF-74. The TGA curve for ZIF-8 presents a significant weight loss at around 420 °C, which

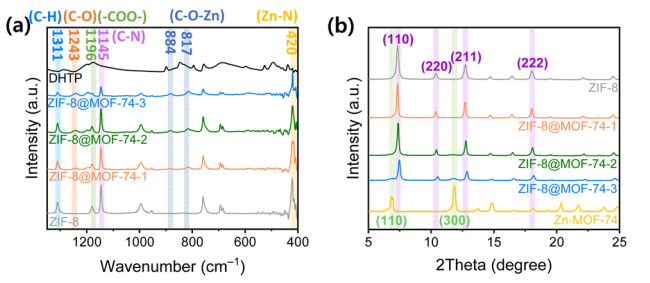

Fig. 1 (a) FT-IR spectra and (b) XRD patterns for DHTA, ZIF-8, and series of ZIF-8@MOF-74 nanoparticles.

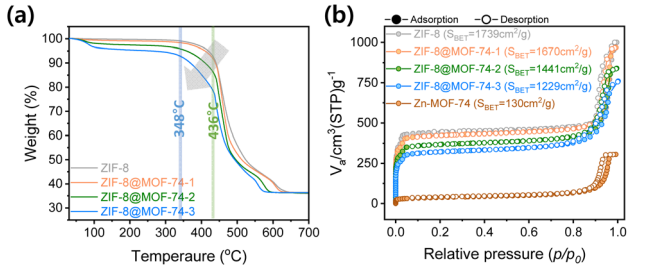

Fig. 2 (a) TGA curves measured under an air atmosphere and (b) N_2 adsorption–desorption isotherms measured at 77 K for the ZIF-8, Zn-MOF-74, and series of ZIF-8@MOF-74 nanoparticles.

is attributable to the collapse of the ZIF-8 architecture and decomposition of the 2MeIM organic ligand. On the other hand, the TGA curve for ZIF-8@MOF-74 exhibits a first-step weight loss at around 350 °C because of the decomposition of DHTA and a second-step weight loss at around 450 °C resulting from the decomposition of 2MeIM. Meanwhile, increasing the Zn-MOF-74 concentration further increased the second-step weight loss because more of the DHTA organic ligand had decomposed. Overall, the TGA curves show that increasing the amount of Zn-MOF-74 decorating the ZIF-8 nanoparticles decreased the thermal stability. Moreover, the final residual weight of zinc oxide in all the materials was approximately 35%, indicating that the Zn ions in the ZIF-8@MOF-74 nanoparticles were retained during the ligand-exchange process.

N_2 adsorption–desorption isotherms were generated to help understand the impact of ligand exchange on the MOF porous structure. The N_2 adsorption–desorption isotherms for ZIF-8 and ZIF-8@MOF-74 nanoparticles in Fig. 2b exhibit type I curves, indicating a structure with narrow micropores.[81,95,96] This suggests that decorating the ZIF-8 structure with Zn-MOF-74 could have slightly modified the pore architecture, resulting in partial pore blockage or modifying the pore distribution and connectivity within the material that reduced the mesopore and micropore volumes, as evidenced in Fig. S4. The Fig. S4 shows a decrease in pore size distribution of the ZIF-8@MOF-74 nanoparticles with an increase in the proportion of Zn-MOF-74, resulting in an increased contribution of micropores and a subsequent decrease in the overall pore volume associated with larger pores. Consequently, the ZIF-8@MOF-74 nanoparticles had a smaller surface area accessible for N_2 adsorption and desorption compared to the ZIF-8 nanoparticles.

The observed decrease in BET surface area and pore size can be rationalized by several coupled effects operating in the MOF-on-MOF architecture. First, the formation of an interface between MOFs with mismatched lattice parameters induces interfacial confinement and structural distortion, which can partially block or constrict pore apertures at the MOF-on-MOF boundary.[97–99] Second, the confinement of the rotation nature of the 2MeIM ligand of ZIF-8 effectively narrows the accessible pore windows relative to the pristine ZIF-8 nanoparticles, thereby reducing the overall accessible microporosity.[100–102] Third, the intrinsically lower BET surface area of Zn-MOF-74 compared to that of ZIF-8, together with the modified pore architecture in the hierarchical composite, is consistent with the experimentally observed shift toward smaller pore sizes in the distribution (Fig. 2b).[103,104] The BET surface area of the ZIF-8 nanoparticles was approximately 1739 $m^2\ g^{-1}$, which is consistent with that previously reported in the literature,[23,82] while those of ZIF-8@MOF-74-1, ZIF-8@MOF-74-2, and ZIF-8@MOF-74-3 were 1670, 1441, and 1229 $m^2\ g^{-1}$, respectively. This corresponds with the observed decrease in pore size distribution (Fig. S4).

The external and internal structural morphologies of ZIF-8 and ZIF-8@MOF-74 nanoparticles were confirmed to demonstrate the Zn-MOF-74 decoration effect on the ZIF-8 nanoparticles. The FE-SEM images in Fig. 3a show that the ZIF-8 nanoparticles exhibit a rhombic dodecahedral structure with a diameter of 50–100 nm.[68,105]

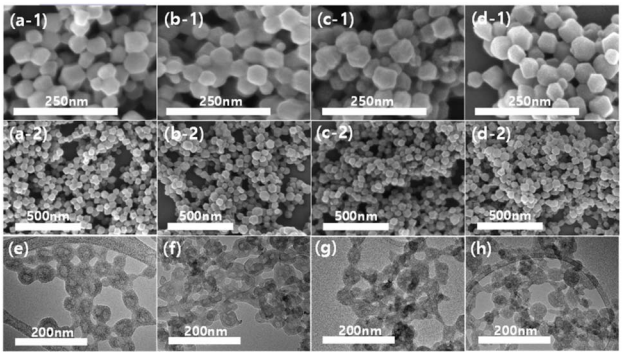

Fig. 3 FE-SEM images of (a) ZIF-8, (b) ZIF-8@MOF-74-1, (c) ZIF-8@MOF-74-2, and (d) ZIF-8@ MOF-74-3 nanoparticles at (1) high and (2) low magnification and TEM images of (e) ZIF-8, (f) ZIF-8@MOF-74-1, (g) ZIF-8@MOF-74-2, and (h) ZIF-8@MOF-74-3 nanoparticles.

The FE-SEM images in Fig. 3b–d exhibit that ZIF-8@MOF-74 nanoparticles maintained the inherent external morphology and size of the ZIF-8 nanoparticles. Meanwhile, the Zn-MOF-74 nanoparticles were well-decorated on the surface of the ZIF-8 nanoparticles. The optical images of ZIF-8 and ZIF-8@MOF-74 powders shown in Fig. S5 show that the initially white ZIF-8 nanoparticles became yellowish ZIF-8@MOF-74 nanoparticles due to the formation of Zn-MOF-74 on the surface of the ZIF-8 nanoparticles *via* the ligand-exchange method from 2MeIM to DHTA. The TEM images in Fig. 3e–h show that the morphologies of the ZIF-8 and ZIF-8@MOF-74 nanoparticles were well-maintained and that the decoration of the ZIF-8 nanoparticle surfaces with Zn-MOF-74 was successful.

In particular, the EDS mapping, HAADF-TEM, HAADF-STEM images, and EELS spectra of ZIF-8 and ZIF-8@MOF-74 nanoparticles, which were shown in Fig. S6–S9, further demonstrate successful Zn-MOF-74 conversion and structure of the ZIF-8@MOF-74 *via* the ligand-exchange process. As a result, although Zn-MOF-74 is concentrated at the ZIF-8 surface, HAADF-TEM and elemental line-scan analyses indicate that the outer layer is not a discrete, uniform shell. Rather, Zn-MOF-74 domains partially penetrate into the ZIF-8 framework, leading to a gradated interfacial region where pore environments from both frameworks coexist. Therefore, the structure is more accurately described as a surface-enriched, interpenetrated composite rather than a classical core–shell configuration.

XPS analysis was performed to identify any modified chemical bonds in the ZIF-8@MOF-74 nanoparticles after DHTA organic ligand incorporation into the ZIF-8 nanoparticles (Fig. 4). To further validate the presence of the DHTA organic ligand in the ZIF-8@MOF-74 nanoparticles, Fig. 4a–d presents a survey XPS spectrum and high-resolution N 1s, O 1s, and Zn 2p spectra for ZIF-8@MOF-74-3 to demonstrate the indication of the Zn-MOF-74 characteristics. The N 1s spectra in Fig. 4b show that the peaks can be deconvoluted into Zn–N and C–N bonds at 398.6 and 397.0 eV in pristine ZIF-8.[106,107] With increasing conversion to Zn-MOF-74, the intensities of these

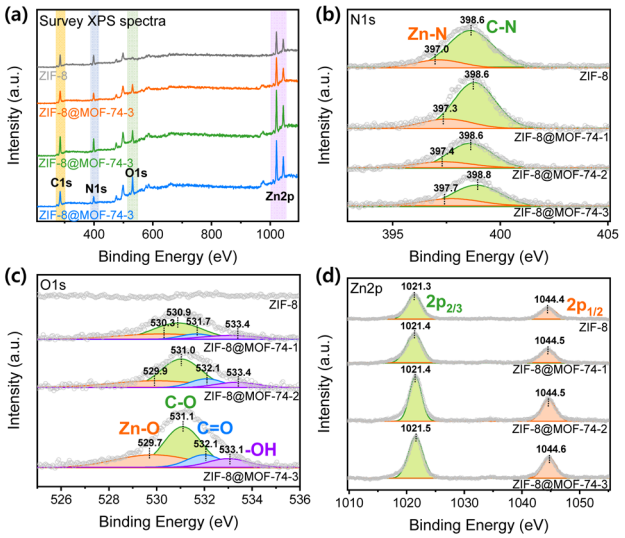

Fig. 4 (a) Survey XPS spectra and high-resolution XPS spectra for the (b) N 1s, (c) O 1s, and (d) Zn 2p of ZIF-8 and series of ZIF-8@MOF-74nanoparticles with deconvolution of the major peak.

deconvoluted peaks progressively decrease, indicating cleavage of Zn–N bonds between Zn^{2+} and the 2MeIM ligand and confirming the removal of 2MeIM. Fig. 4c presents the O 1s spectra, which confirm the incorporation of the DHTA linker and the formation of the Zn-MOF-74 structure. Pure ZIF-8 shows essentially no O 1s signal, whereas the O 1s peak grows steadily with increasing conversion to Zn-MOF-74, consistent with the introduction of oxygen-containing DHTA ligands. The spectrum was deconvoluted into four peaks at 533.4, 531.7, 530.9, and 530.3 eV, corresponding to –OH, C–O, C═O, and Zn–O bonds, respectively.[103,108–110] Moreover, the Zn 2p spectra in Fig. 4d show that the peak areas of Zn $2p_{3/2}$ and Zn $2p_{1/2}$ at 1044.4 and 1021.3 eV for ZIF-8 and increase with higher Zn-MOF-74 conversion. The observed increase in Zn 2p peak intensity and area with higher conversion indicates enhanced surface exposure of Zn^{2+} characteristic of the Zn-MOF-74 with open metal sites.[103,111]

To confirm the presence of open metal sites and evaluate the sorption ability of incorporation of Zn-MOF-74, gas sorption isotherms measured at 308.15 K for pristine ZIF-8 and ZIF-8@MOF-74-3 are presented in Fig. S10. The H_2 sorption isotherms show negligible uptake for both samples, indicating minimal interaction with small molecules such as H_2 (2.9 Å) (Fig. S10a). In contrast, the adsorption capacities of larger gases, including N_2 (3.6 Å) and CH_4 (3.8 Å), were reduced in ZIF-8@MOF-74-3 compared to pristine ZIF-8 (Fig. S10b and c). This decrease is attributed to the effective narrowing of the pore aperture and capacity upon formation of the Zn-MOF-74. This phenomenon is shown specifically as a result of the N_2 sorption isotherm (Fig. S10b). While pristine ZIF-8 exhibits a flexible pore window capable of accommodating gases up to ~3.8 Å through gate-opening of the 2MeIM linkers, the incorporation of the rigid Zn-MOF-74 suppresses this gate-opening behavior resulting in a fixed pore aperture of approximately 3.4 Å that restricts N_2 and CH_4 transport and this results were corresponding to the N_2 adsorption–desorption isotherm as shown in Fig. 2b.[44,112,113]

Notably, unlike N_2 and CH_4, the CO_2 sorption is enhanced, especially at low pressures for ZIF-8@MOF-74-3 (Fig. S10d), providing evidence of CO_2 affinity arising from the open metal sites in the Zn-MOF-74.[114,115] These results confirm the successful incorporation of the DHTA organic ligand in the ZIF-8@MOF-74 nanoparticles.[108–110] However, the increase in intrinsic CO_2 sorption capacity is relatively modest and therefore cannot solely account for the enhanced gas separation performance. Instead, the primary role of the open metal sites is to promote stronger interfacial interactions with the polymer matrix, particularly through coordination interactions and hydrogen bonding with the carboxylic acid functionalities of 6FDD. These interactions enhance MOF-polymer compatibility and suppress the formation of non-selective interfacial voids.

Characterization of the ZIF-8 and ZIF-8@MOF-74 MMMs

ZIF-8 or ZIF-8@MOF-74 nanoparticles were incorporated into a 6FDD polyimide matrix to form an MMM. Of note, the actual MOF nanoparticle loading was estimated from back-calculations reported in Table S1 based on the TGA curves shown in Fig. S11. Of particular interest, the carboxylic acid functionality of the 6FDD polyimide can interact with the hydroxyl group of the DHTA organic ligand and open metal sites of Zn-MOF-74, resulting in enhanced MOF-polymer compatibility and thereby reducing interfacial defects in the MMMs.

Fig. 5a presents XRD patterns for the pure 6FDD polyimide membrane and the 20 wt% ZIF-8 and ZIF-8@MOF-74 based MMMs. That for the pure 6FDD polyimide membrane exhibits

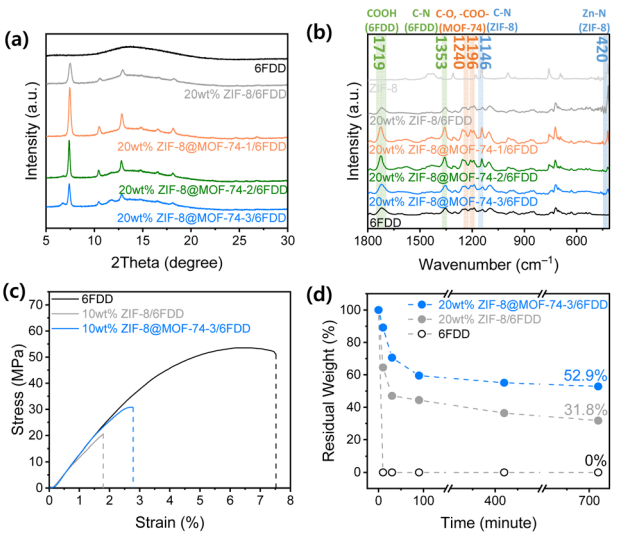

Fig. 5 (a) XRD patterns and (b) FT-IR spectra for the pure 6FDD polyimide membrane and the 20 wt% ZIF-8/6FDD, ZIF-8@MOF-74-1/6FDD, ZIF-8@MOF-74-2/6FDD, and ZIF-8@MOF-74-3/6FDD MMMs. (c) Stress–strain curves for the pure 6FDD polyimide membrane and the 10 wt% ZIF-8/6FDD and ZIF-8@MOF-74-3/6FDD MMMs. (d) Dissolution testing results for the pure 6FDD polyimide membrane and the 20 wt% ZIF-8/6FDD and ZIF-8@MOF-74-3/6FDD MMMs.

a broad peak at $2\theta = 13.6°$, thereby confirming its amorphousness. The *d*-spacing value for the pure 6FDD polyimide membrane of approximately 3.27 Å (using Bragg's equation based on the center location of the broad peak) provides the average polymer chain distance, which is related to the gas transport properties discussed later. The XRD pattern for the 20 wt% ZIF-8/6FDD MMM reveals distinct crystalline peaks corresponding to the intrinsic ZIF-8 crystal phase combined with broad amorphous peaks due to the 6FDD polyimide matrix. As the Zn-MOF-74 decoration concentration was increased, the XRD patterns for the ZIF-8@MOF-74 based MMMs show that the crystalline peak for the ZIF-8 nanoparticles was preserved but with decreasing peak intensity, while a new crystalline peak corresponding to Zn-MOF-74 formation increased. This result supports that the Zn-MOF-74 decoration was well-formed on the ZIF-8 nanoparticles and proportional to the Zn-MOF-74 concentration. Thus, the uniform series of ZIF-8@MOF-74/6FDD MMMs were formed without destroying the inherent MOF crystallinity and amorphous region of 6FDD polyimide.

Fig. 5b shows FT-IR spectra for the ZIF-8 nanoparticles, pure 6FDD polyimide membrane, 20 wt% ZIF-8/6FDD and series of ZIF-8@MOF-74/6FDD MMMs. The pure 6FDD polyimide membrane contains absorption bands at 1353 and 1719 cm^{-1} due to C–N and COOH, respectively. Meanwhile, that for the ZIF-8 nanoparticles exhibits characteristic peaks at 1146 cm^{-1} for the C–N bond in the imidazole ring and 420 cm^{-1} for the Zn–N bond. In addition, the peak intensity of the Zn–N bond increased with increasing MOF weight loading in the MMM (Fig. S12a). The FT-IR spectra for the series of 20 wt% ZIF-8@MOF-74/6FDD MMMs in Fig. 5b show that the characteristic peaks pertaining to ZIF-8 were preserved even after Zn-MOF-74 decoration on the ZIF-8 nanoparticles *via* the ligand-exchange method. Meanwhile, the peaks at 1240 and 1196 cm^{-1} corresponding to the C–O and –COO– groups of the DHTA ligand in the Zn-MOF-74 became larger as the Zn-MOF-74 conversion amount was increased. This suggests a strong interaction between the carboxyl group in the 6FDD polymer matrix and the hydroxyl groups and open metal sites of Zn-MOF-74, as evidenced by a significant peak shift for the carboxyl group in the FT-IR spectra in Fig. S12b. Indeed, the peak shift was more noticeable for the 20 wt% Zn-MOF-74 MMM (from 1725 to 1721 cm^{-1}).

Fig. 5c and d illustrate the enhanced mechanical and chemical stability of the series of 20 wt% ZIF-8@MOF-74/6FDD MMMs compared to the ZIF-8/6FDD MMM and the pure 6FDD polyimide membrane. Fig. 5c presents stress–strain curves obtained from UTM measurements to show the mechanical properties of the pure 6FDD membrane and 10 wt% ZIF-8/6FDD and ZIF-8@MOF-74-3/6FDD MMMs. The corresponding mechanical parameter values are summarized in Table S2. The pure 6FDD polyimide membrane shows a tensile strength of 53.6 MPa and elongation-at-break of 7.5%, thereby demonstrating the robustness of the self-standing film. Compared to the 6FDD polyimide membrane, the 10 wt% ZIF-8/6FDD MMM exhibited a reduced tensile strength (20.6 MPa) and elongation-at-break (1.8%), thereby reflecting its relative brittleness attributable to the incorporation of rigid MOF fillers into the polymer matrix. However, the 10 wt% ZIF-8@MOF-74-3/6FDD MMM showed enhanced tensile strength and elongation-at-break compared to the 10 wt% ZIF-8/6FDD MMM, even for the same MOF weight loading. These results reflect that ZIF-8@MOF-74 showed a favourable interaction between Zn-MOF-74 and the 6FDD polymer matrix that improved the mechanical properties of the resulting MMM.

To demonstrate the chemical stability of the membranes, dissolution testing was performed by immersing the pure 6FDD membrane and the 20 wt% ZIF-8/6FDD and ZIF-8@MOF-74-3/6FDD MMMs in THF solvent (Fig. 5d). The pure 6FDD polyimide membrane immediately dissolved when it was immersed in THF due to its good solvent solubility. On the other hand, the 20 wt% ZIF-8/6FDD and ZIF-8@MOF-74-3/6FDD MMMs did not show such a sudden residual weight loss, thus indicating their enhanced chemical stability toward the THF solvent. After 30 hours (720 min), the 20 wt% ZIF-8@MOF-74-3/6FDD MMM had a residual weight of 52.9%, which is much higher than that of the 20 wt% ZIF-8/6FDD MMM (31.8%). Enhanced chemical stability arises from interfacial interactions between the carboxylate groups of 6FDD and the hydroxyl ligands and open metal sites of Zn-MOF-74, which are known to promote hydrogen bonding and coordination with carboxyl-functional polymers.[71–73]

Fig. 6 and S13 show cross-sectional SEM and optical images of the 20 wt% ZIF-8/6FDD and series of ZIF-8@MOF-74/6FDD MMMs, respectively. For comparison, optical and cross-sectional SEM images of the pure 6FDD polyimide membrane are shown in Fig. S14. The cross-sectional SEM images of the 20 wt% ZIF-8/6FDD MMM in Fig. 6a show the distribution of the MOF nanoparticles in the 6FDD polyimide matrix, but we can also see an aggregated MOF-rich portion at the bottom of the images, which is possibly due to the low MOF-polymer compatibility (Fig. S15a). Of note, MOF weight loading surpassing 30 wt% in an MMM resulted in an agglomerated MOF-polymer composite due to a significantly increased MOF-polymer interfacial interaction. Thus, we decided to fabricate 10 and 20 wt% MMMs to systematically investigate the effects of Zn-MOF-74 decoration on ZIF-8 nanoparticles on the gas transport properties and polymer chain stability of the resulting MMMs.

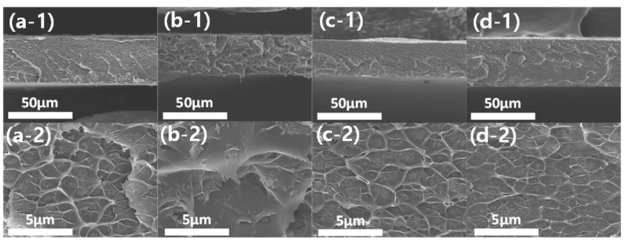

Fig. 6 Cross-sectional SEM images of (a) 20 wt% ZIF-8/6FDD, (b) 20 wt% ZIF-8@MOF-74-1/6FDD, (c) 20 wt% ZIF-8@MOF-74-2/6FDD, and (d) 20 wt% ZIF-8@MOF-74-3/6FDD MMMs, (1) full range and (2) middle part of the MMM.

Of particular interest, the images of the 20 wt% ZIF-8@MOF-74-3 MMM in Fig. 6d show well-dispersed ZIF-8@MOF-74 nanoparticles without any noticeable defects across the entire film from the bottom side to the top side. This is due to the good MOF-polymer interfacial interaction in the MMM resulting from interactions between the hydroxyl group in DHTA and the carboxyl group in 6FDD, as well as the open metal sites in Zn-MOF-74 and the carboxyl group in 6FDD. To investigate the interaction between the MOF and polymer in the MMMs, a compatibility test between them was performed by stirring ZIF-8 and ZIF-8@MOF-74 nanoparticles overnight in a 6FDD polymer solution (Fig. S16). The ZIF-8 dispersion remained stable, exhibiting a uniform suspension in the polymer solution. In contrast, ZIF-8@MOF-74 nanoparticles showed significant aggregation, attributed to strong interactions between the carboxylate groups of the 6FDD polymer and the hydroxyl groups and open metal sites present on the ZIF-8@MOF-74 surface.

Moreover, to probe the strength of polymer-MOF interfacial adhesion, DHTA ligands and Zn-MOF-74 nanoparticles were individually dispersed in the polymer solution (Fig. S16). The DHTA ligands produced clear and homogeneous suspension, whereas the Zn-MOF-74 nanoparticles exhibited pronounced aggregation, indicating that the high density of open metal sites in Zn-MOF-74 shows a strong interaction with the carboxylic acid groups in the polymer matrix. Consequently, the series of 20 wt% ZIF-8@MOF-74/6FDD MMMs demonstrated improved MOF dispersion within the polymer matrix as the Zn-MOF-74 conversion ratio was increased, as particularly evidenced by the reduced sedimentation of MOF particles observed at the bottom of the membrane (Fig. S16a–d). To provide more direct evidence of the interfacial interaction between the 6FDD polymer and ZIF-8@MOF-74 nanoparticles, XPS and DSC analyses were performed (Fig. S17 and S18). The binding energy shifts in C 1s, O 1s, and Zn 2p spectra, coupled with the T_g increase at 20 wt% loading, indicate interfacial interaction and constrained polymer chain mobility *via* coordination bonding between the open metal sites in Zn-MOF-74 and the carboxylic group in 6FDD polymer matrix. The combined results from both analyses consistently support strengthened interaction between the MOF-polymer interfaces.[23,116–121]

Gas permeation properties of the ZIF-8 and ZIF-8@MOF-74 MMMs

To understand the effect of the Zn-MOF-74 decoration on ZIF-8 nanoparticles in 6FDD-based MMMs in terms of the gas transport properties, pure gas permeation tests were conducted for H_2, N_2, CH_4, and CO_2 gases at 15 psi and 35 °C (Fig. 7, S19, and Table 1). The ZIF-8/6FDD MMM showed better H_2 and CO_2 permeabilities compared to those of the pure 6FDD polyimide membrane due to the enhanced molecular transport through the intrinsically porous ZIF-8 architecture. Surprisingly, the series of ZIF-8@MOF-74/6FDD MMMs exhibited a significant enhancement in H_2 and CO_2 permeabilities relative to those of the ZIF-8/6FDD MMM. In particular, the ZIF-8@MOF-74-1/6FDD MMM revealed an approximately 800% increase in CO_2 permeability compared to that of the pure 6FDD polyimide membrane. However, the ZIF-8@MOF-74-1 and ZIF-8@MOF-74-3 based MMMs with a higher concentration of Zn-MOF-74 used to decorate the ZIF-8 nanoparticles had slightly decreased H_2 and CO_2 permeabilities, possibly due to the reduced surface areas of ZIF-8@MOF-74-2 and ZIF-8@MOF-74-3, as confirmed by the N_2 isotherm analysis mentioned previously. Even so, the ZIF-8@MOF-74-3/6FDD MMM still showed higher H_2 and CO_2 permeabilities compared to those of the ZIF-8/6FDD MMM with the same MOF weight loading. This is because the higher pore window of Zn-MOF-74, and subsequently the Zn-MOF-74-decorated ZIF-8 architecture, can significantly enhance the diffusion of gas molecules through the MMM. The intrinsic open metal sites of Zn-MOF-74 can further increase the number of gas sorbing sites, which is related to the gas solubility in the MMMs.[122–125] In addition, the good compatibility and interaction between ZIF-8@MOF-74 and the 6FDD polyimide matrix led to uniform MOF dispersion and could have caused well-controlled 6FDD polymer chain entanglement at the MOF-polymer interface. ZIF-8 nanoparticles, thereby effectively narrowing the pore window.[122–125] This feature can increase the ideal gas selectivity, thereby further improving the gas transport properties.

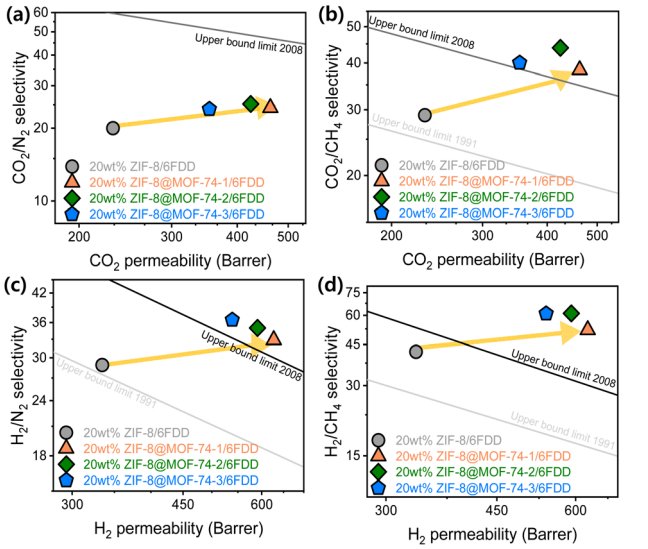

Fig. 7 (a) CO_2/N_2, (b) CO_2/CH_4, (c) H_2/N_2, and (d) H_2/CH_4 gas separation performances of pristine 6FDD membrane, ZIF-8/6FDD and series of ZIF-8@MOF-74/6FDD MMMs with 20 wt% MOF loading at 15 psi and 35 °C with the upper-bound limits.

To elucidate the engineered gas transport properties of the Zn-MOF-74-decorated ZIF-8 incorporated MMMs, we decoupled their N_2, CH_4, and CO_2 permeabilities into diffusivities and solubilities and the corresponding diffusivity-selectivity and solubility-selectivity parameters (Fig. S20 and Tables S3, S4). The H_2 diffusivity and solubility were excluded due to the extremely short time lag, which precluded reliable diffusivity calculation void. Fig. S20a shows that the CO_2 diffusivities for the ZIF-8@MOF-74/6FDD MMMs significantly increased compared to that for the ZIF-8/6FDD MMM owing to the

Table 1 Gas permeation properties of the membranes. (the permeability (P) values are in Barrers, the number of independent membrane samples tested $n = 4$)

Sample	$P(H_2)$	$P(N_2)$	$P(CH_4)$	$P(CO_2)$	$P(H_2)/P(CO_2)$	$P(CO_2)/P(N_2)$	$P(CO_2)/P(CH_4)$	$P(H_2)/P(N_2)$	$P(H_2)/P(CH_4)$
6FDD	106 ± 6	4.5 ± 0.3	3.7 ± 0.2	116 ± 7	0.914 ± 0.003	25.8 ± 0.2	31.3 ± 0.2	23.7 ± 0.3	28.6 ± 0.1
10 wt% ZIF-8/6FDD	149 ± 7	5.7 ± 0.3	4.0 ± 0.2	125 ± 6	1.192 ± 0.001	21.9 ± 0.1	31.3 ± 0.1	26.1 ± 0.1	37.3 ± 0.1
10 wt% ZIF-8@MOF-74-1/6FDD	354 ± 20	12.4 ± 0.7	8.3 ± 0.5	308 ± 17	1.149 ± 0.002	25.7 ± 0.1	37.1 ± 0.2	29.5 ± 0.1	42.7 ± 0.2
10 wt% ZIF-8@MOF-74-2/6FDD	348 ± 15	11.8 ± 0.6	7.7 ± 0.3	281 ± 12	1.238 ± 0.005	23.8 ± 0.1	36.5 ± 0.1	29.5 ± 0.1	45.2 ± 0.2
10 wt% ZIF-8@MOF-74-3/6FDD	304 ± 11	10.2 ± 0.4	6.6 ± 0.2	249 ± 9	1.221 ± 0.001	24.9 ± 0.1	37.6 ± 0.2	30.4 ± 0.1	45.9 ± 0.3
20 wt% ZIF-8/6FDD	335 ± 14	11.6 ± 0.5	8.0 ± 0.3	232 ± 10	1.444 ± 0.002	19.30.1	29.0 ± 0.2	27.9 ± 0.2	41.9 ± 0.2
20 wt% ZIF-8@MOF-74-1/6FDD	627 ± 28	19.1 ± 0.9	12.0 ± 0.5	463 ± 21	1.354 ± 0.001	24.4 ± 0.1	38.6 ± 0.1	33.0 ± 0.1	52.2 ± 0.2
20 wt% ZIF-8@MOF-74-2/6FDD	591 ± 31	17.0 ± 1.0	9.7 ± 0.5	424 ± 23	1.394 ± 0.003	24.9 ± 0.1	43.7 ± 0.1	34.8 ± 0.1	60.9 ± 0.1
20 wt% ZIF-8@MOF-74-3/6FDD	539 ± 22	15.0 ± 0.6	8.9 ± 0.4	354 ± 15	1.523 ± 0.002	23.6 ± 0.1	39.8 ± 0.1	35.9 ± 0.1	60.6 ± 0.3

intrinsically larger pore size in the Zn-MOF-74-decorated ZIF-8 crystalline structure. However, the ZIF-8@MOF-74/6FDD MMMs showed decreased CO_2 diffusivity with an increase in Zn-MOF-74 concentration, because of the reduced surface area. The corresponding gas solubilities for the ZIF-8@MOF-74/6FDD MMMs are shown in Fig. S20b. Those for the 20 wt% ZIF-8@MOF-74/6FDD MMMs were lower than those for the 20 wt% ZIF-8/6FDD MMM, which is possibly due to the decreased surface area and enhanced MOF-polymer interfacial compatibility. Meanwhile, the 20 wt% ZIF-8@MOF-74/6FDD MMMs presented increased CO_2/N_2 and CO_2/CH_4 solubilities due to the open metal sites in Zn-MOF-74 increasing selective gas sorption (*i.e.*, CO_2-favorable sites). Fig. S20c shows the diffusivities and diffusivity-selectivity values for the pure 6FDD polyimide, ZIF-8/6FDD MMMs, and ZIF-8@MOF-74-3/6FDD MMMs with various MOF weight loadings. The N_2, CH_4, and CO_2 diffusivities increased for both the ZIF-8/6FDD and ZIF-8@MOF-74-3/6FDD MMMs compared to those for the pure 6FDD polyimide membrane owing to the incorporation of intrinsically porous MOF nanoparticles. Moreover, the ZIF-8@MOF-74-3/6FDD MMMs exhibited relatively higher diffusion values than the ZIF-8/6FDD MMM, resulting from the large pore-sized Zn-MOF-74 decoration. Notably, the CO_2/CH_4 diffusivity-selectivity values for the ZIF-8@MOF-74-3/6FDD MMMs increased as the MOF weight loading was increased, despite the larger pore size of the Zn-MOF-74 component. This enhancement is attributed to the preservation of the ZIF-8 structure within the ZIF-8@MOF-74 nanoparticles, which has an appropriate pore size (3.4 Å) for separating CO_2 based on its kinetic diameter (3.3 Å). In addition, the inserted Zn-MOF-74 crystalline structure could have assisted in preventing the rotational freedom of the 2MeIM organic ligand in the ZIF-8 nanoparticles, thereby effectively narrowing the pore window.[126] Fig. S20d and Table S5 presents the solubilities and solubility-selectivity values for the pure 6FDD polyimide membrane and the ZIF-8/6FDD and ZIF-8@MOF-74-3/6FDD MMMs with various MOF weight loadings. The solubilities for the ZIF-8@MOF-74-3/6FDD MMM decreased with an increase in MOF loading, likely due to enhanced compatibility between the carboxyl groups in 6FDD and the open metal sites and hydroxyl groups in ZIF-8@MOF-74-3.

The temperature dependence of CO_2 permeability (35 to 95 °C) was investigated to evaluate transport barriers (Fig. S21). Pristine 6FDD shows a positive activation energy (E_p = +2.7 kJ mol^{-1}), while the incorporation of ZIF-8 reduces E_p to +0.24 kJ mol^{-1}, indicating lowered diffusion resistance *via* microporous pathways. Notably, 20 wt% ZIF-8@MOF-74-3 MMM exhibit the lowest value (E_p = −1.38 kJ mol^{-1}). This significant and unusual reduction to a negative value suggests that the defect-free interface and MOF-dominated transport channels effectively minimize the energy barrier for CO_2 permeation, surpassing the performance of both pristine polymer and ZIF-8-based membranes.[127–130]

Physical aging commonly occurs in glassy polymers, where polymer chains gradually relax toward thermodynamic equilibrium.[131,132] During this process, polymer mobility becomes increasingly restricted, free volume within the polymer matrix decreases, and gas permeability declines over long-term operation, ultimately leading to deterioration of membrane performance. To evaluate long-term stability, aging tests were conducted for pristine 6FDD, 20 wt% ZIF-8/6FDD, and series of ZIF-8@MOF-74/6FDD MMMs (Fig. S22) for H_2, N_2, CH_4, and CO_2 gases. While pristine 6FDD exhibited a gradual decline in gas permeability over time, the incorporation of MOF fillers mitigated the aging effect. In particular, the ZIF-8@MOF-74-containing MMMs maintained higher permeability for all tested gases compared to pristine 6FDD. Notably, the 20 wt% ZIF-8@MOF-74-1 MMM exhibited negligible permeability loss during the aging period, demonstrating the most stable performance among the MMMs and highlighting its outstanding long-term stability.

Table S6 presents pure- and mixed-gas transport properties of CO_2 and CH_4 in pristine 6FDD membrane and 20 wt% ZIF-8@MOF-74-1/6FDD MMM. For the 6FDD membrane, compared to the pure-gas results, the mixed-gas CO_2 and CH_4 permeabilities are ∼10 and ∼25% higher, respectively, resulting in slightly lower mixed-gas CO_2/CH_4 selectivity. This result can be attributed to CO_2-induced plasticization under mixed-gas conditions, where the presence of CO_2 enhances polymer chain mobility and facilitates the transport of co-permeating CH_4.[133] In contrast, no significant CO_2-induced plasticization is observed in the MMM. For example, the mixed-gas CO_2 and CH_4 permeabilities (520 and 13.1 Barrer) are slightly lower than the corresponding pure-gas values (540 and 15.2 Barrer), with the effect being more noticeable for CH_4. In addition, the mixed-gas selectivity (∼40) is also slightly higher than the pure-

gas selectivity (~36), indicating competitive sorption effects between CO_2 and CH_4.[134] These results suggest strong potential for industrial deployment under practical operating conditions.

The series of ZIF-8@MOF-74/6FDD MMMs showed significantly enhanced gas permeabilities compared to the theoretical values predicted by applying the Maxwell model (Fig. S23). The model provides an upper limit for H_2 and CO_2 gas permeabilities by assuming that ZIF-8 is infinitely permeable and a lower limit based on ZIF-8 being impermeable. The 10 wt% ZIF-8/6FDD MMM exhibited permeability within these predicted boundaries, whereas the series of ZIF-8@MOF-74/6FDD MMMs surpassed the upper limit, thus suggesting significant enhancement of the gas transport properties therein. We compared gas separation performances of CO_2/CH_4 and H_2/CH_4 for series of 20 wt% ZIF-8@MOF-74/6FDD MMMs with those of other materials previously reported in the literature for ZIF-8-, M-MOF-74- and PIM-1-based MMMs (Fig. S24 and Table S7). The series of ZIF-8@MOF-74/6FDD MMMs exhibit higher (or comparable) gas separation performances that surpass the 2008 upper-bound limits. This is consistent with the series of ZIF-8@MOF-74/6FDD MMMs based on MOF-polymer interfacial engineering, which are promising candidates for CO_2 and H_2 separation membranes.

Plasticization can occur when a polymer membrane is exposed to highly soluble gases (*e.g.*, CO_2) at a high feed pressure, which relaxes the polymer chains and significantly decreases the gas-separation performance under realistic conditions.[6,7,135] To evaluate the membrane stability under high-pressure CO_2,[6,136] Fig. 8 presents normalized CO_2 permeability as a function of feed gas pressure up to 750 psi at 35 °C for the pure 6FDD polyimide membrane and the 10 and 20 wt% ZIF-8/6FDD and series of ZIF-8@MOF-74/6FDD MMMs. The pure 6FDD polyimide membrane shows a 4.5-fold normalized CO_2 permeability at 750 psi, indicating significantly relaxed polymer chains that can lead to non-selective voids between the MOF filler and polymer matrix. The 20 wt% ZIF-8/6FDD MMM exhibited a slightly lower normalized CO_2 permeability at 750 psi due to the relatively enhanced polymer chain rigidity caused by the proximity of neighbouring rigid MOF nanoparticles. On the other hand, the series of 20 wt% ZIF-8@MOF-74/6FDD MMMs revealed significantly reduced normalized CO_2 permeability at 750 psi. Interestingly, the normalized CO_2 permeability at 750 psi of the 20 wt% ZIF-8@MOF-74-3/6FDD MMM was less than 3-fold of the pure 6FDD polyimide membrane.

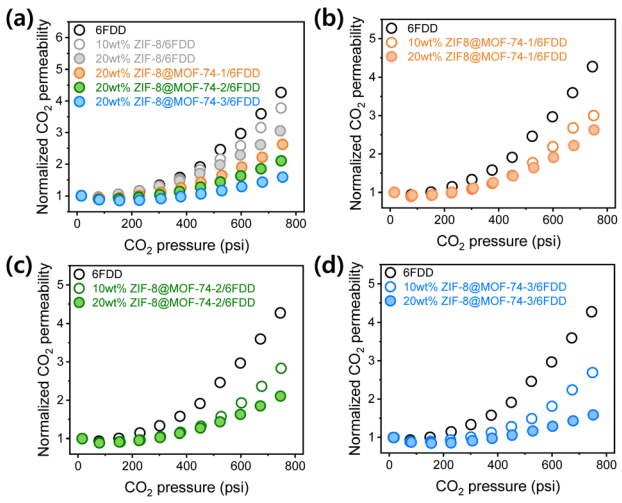

Fig. 8 Normalized CO_2 permeability as a function of feed gas pressure: (a) all of the pure 6FDD polyimide membrane and the 10 and 20 wt% ZIF-8/6FDD and 20 wt% ZIF-8@MOF-74/6FDD MMMs, (b) the pure 6FDD polyimide membrane and the 10 and 20 wt% ZIF-8@MOF-74-1/6FDD MMMs, (c) the pure 6FDD polyimide membrane and the 10 and 20 wt% ZIF-8@MOF-74-2/6FDD MMMs, and (d) the pure 6FDD polyimide membrane and the 10 and 20 wt% ZIF-8@MOF-74-3/6FDD MMMs.

Plasticization pressure is defined as the minimum permeability pressure that occurs due to the saturation of sorption sites, resulting in polymer chain swelling and showing a minimum permeability pressure where the polymer matrix begins to lose its rigid, glassy characteristic and transitions toward a rubbery state (decrease of T_g), leading to a sharp increase in gas permeability accompanied by a sharp deterioration in selectivity.[6,7,135] As shown in Fig. 8a, the pristine 6FDD membrane exhibits a plasticization pressure of approximately ~77 psi, which remains unchanged upon incorporation of 20 wt% ZIF-8. In contrast, incorporation of ZIF-8@MOF-74 significantly shifts the plasticization pressure to higher values. The plasticization pressure increases to approximately ~112 psi for the 20 wt% ZIF-8@MOF-74-1 MMM (Fig. 8a) and further to approximately ~200 psi for the 20 wt% ZIF-8@MOF-74-3 MMM (Fig. 8d). This progressive increase supports MOF-74 decoration, which effectively suppresses CO_2-induced plasticization, due to enhancing interfacial compatibility and restricting polymer chain mobility. This is because the Zn-MOF-74 decoration on the ZIF-8 nanoparticles can develop strong interactions with the 6FDD polyimide matrix. These occur between the hydroxyl groups in the DHTA ligand and the carboxyl groups in 6FDD, as well as between the open metal sites in Zn-MOF-74 and the carboxyl group in 6FDD. As a result, the Zn-MOF-74-decorated ZIF-8/6FDD MMM effectively suppresses high-pressure CO_2 plasticization behaviour, thus indicating that it is a good candidate for stable gas separation in industrial applications.

Conclusions

We developed a facile approach to grow Zn-MOF-74 on ZIF-8 nanoparticles using a straightforward ligand-exchange method based on the same metal ion (Zn), which partially modified the crystalline structure of ZIF-8 nanoparticles, enlarged the pore window, and provided open metal sites. Given the carboxyl group of the 6FDD polyimide matrix, ZIF-8@MOF-74 favourably interacted with the 6FDD polymer based on the hydroxyl group of the DHTA ligand and the open metal sites. Thus, the series of ZIF-8@MOF-74 based MMMs showed improved mechanical and chemical stability compared to their ZIF-8/6FDD counterparts with the same MOF weight loading. In addition, ZIF-8@MOF-74 was uniformly dispersed in the 6FDD polymer matrix across the entire film, as revealed *via* cross-

sectional SEM. ZIF-8@MOF-74 based MMMs exhibited a significant enhancement in gas permeability relative to the ZIF-8/6FDD MMMs. The remarkably increased gas permeability of the former surpassed the theoretical permeability predicted by applying the Maxwell model. This phenomenon possibly resulted from the partially inserted Zn-MOF-74 crystalline structure into the ZIF-8 nanoparticles, which enlarged the pore window and rigidified the 2MeIM ligand rotation in the integrated MOF architecture.

Moreover, ZIF-8@MOF-74 interacted favourably with the 6FDD polyimide matrix, thereby creating a modified polymer chain structure. Of practical importance, the ZIF-8@MOF-74 based MMMs showed enhanced high-pressure CO_2 plasticization resistance compared to the pure 6FDD polyimide and ZIF-8/6FDD MMMs. Good interaction between ZIF-8@MOF-74 and the 6FDD polyimide matrix remarkably reduced polymer chain mobility, thereby preventing polymer chain relaxation under high CO_2 feed pressure. Hence, the MOF-on-MOF strategy effectively increases the molecular transport properties and physicochemical stability of the MMM, thereby suggesting the suitability of our engineering approach for fabricating industrial gas-separation membranes.

Author contributions

Jin Hui Jo: conceptualization, methodology, formal analysis, investigation, writing – original draft. Jieun Lee: formal analysis. Eun Ji An: formal analysis. Hyomin Choi: formal analysis. Hyunmo Jae: data curation, formal analysis, investigation. Yubin Lee: formal analysis, Miso Kang: data curation, formal analysis, Jaesung Park: data curation, formal analysis, Hyuk Taek Kwon: formal analysis, Chanmin Lee: methodology, data curation, investigation. Dongkyu Rho: supervision, project administration, writing-review&editing, funding acquisition. Won Seok Chi: conceptualization, supervision, project administration, writing – review & editing, funding acquisition.

Conflicts of interest

There are no conflicts to declare.

Data availability

All data supporting the findings of this study are available from the corresponding authors upon reasonable request.

Supplementary information (SI): detailed experimental methods for Zn-MOF-74 synthesis, crystal structures of ZIF-8 and Zn-MOF-74, mixed gas test, gas permeation parameter estimation, error propagation, Maxwell model calculations, Arrhenius plots and long-term stability of membranes as well as extensive characterization data (*e.g.*, FE-SEM, FT-IR, PSD, optical image of powder and membranes, compatibility test between MOFs and polymer, EDS, HAADF-TEM images, gas sorption isotherms for MOFs, EELS, TGA, XPS, DSC spectra for membranes) and supporting figures and tables. See DOI: https://doi.org/10.1039/d5ta07747h.

Acknowledgements

This study was supported by the Basic Science Research Program through the National Research Foundation (NRF) of Korea funded by the Ministry of Education (RS-2023-00248504), the Korean Institute of Energy Technology Evaluation and Planning (KETEP) and the Ministry of Trade, Industry & Energy (MOTIE) of the Republic of Korea (20229A10100170), the Korean Basic Science Institute (National Research Facilities and Equipment Center) grant funded by the Korean government (MSIT) (RS-2024-00404069), the Korea Evaluation Institute of Industrial Technology (KEIT) through a grant (RS-2025-02316752), funded by the MOTIE, Republic of Korea, and the Korean Basic Science Institute under the R&D program (Project No. C513550) supervised by the Ministry of Science and ICT.

Notes and references

1 M. Galizia, W. S. Chi, Z. P. Smith, T. C. Merkel, R. W. Baker and B. D. Freeman, *Macromolecules*, 2017, **50**, 7809.
2 R. W. Baker, *Ind. Eng. Chem. Res.*, 2002, **41**, 1393.
3 D. S. Sholl and R. P. Lively, *Nature*, 2016, **532**, 435.
4 D. F. Sanders, Z. P. Smith, R. Guo, L. M. Robeson, J. E. McGrath, D. R. Paul and B. D. Freeman, *Polymer*, 2013, **54**, 4729.
5 L. M. Robeson, *J. Membr. Sci.*, 2008, **320**, 390.
6 J. W. Kim, J. H. Jo, S. Jeong, W. S. Chi and H. Kim, *Chem. Commun.*, 2023, **59**, 6987.
7 A. F. Ismail and W. Lorna, *Sep. Purif. Technol.*, 2002, **27**, 173.
8 W. S. Chi, B. J. Sundell, K. Zhang, D. J. Harrigan, S. C. Hayden and Z. P. Smith, *ChemSusChem*, 2019, **12**, 2355.
9 J. Lee, S. Jeon, E. Ji An, H. Gwon Kim, J. Hui Jo, N. Han, S. Park and W. Seok Chi, *Sep. Purif. Technol.*, 2025, **356**, 129854.
10 H. Lee, W. S. Chi, M. J. Lee, K. Zhang, F. Edhaim, K. Mizrahi Rodriguez, S. J. A. DeWitt and Z. P. Smith, *Adv. Funct. Mater.*, 2022, **32**, 2207775.
11 Q. Qian, A. X. Wu, W. S. Chi, P. A. Asinger, S. Lin, A. Hypsher and Z. P. Smith, *ACS Appl. Mater. Interfaces*, 2019, **11**, 31257.
12 H. Furukawa, K. E. Cordova, M. O'Keeffe and O. M. Yaghi, *Science*, 2013, **341**, 1230444.
13 Q. Qian, P. A. Asinger, M. J. Lee, G. Han, K. Mizrahi Rodriguez, S. Lin, F. M. Benedetti, A. X. Wu, W. S. Chi and Z. P. Smith, *Chem. Rev.*, 2020, **120**, 8161.
14 J. Liu, T. A. Goetjen, Q. Wang, J. G. Knapp, M. C. Wasson, Y. Yang, Z. H. Syed, M. Delferro, J. M. Notestein, O. K. Farha and J. T. Hupp, *Chem. Soc. Rev.*, 2022, **51**, 1045.
15 L. E. Kreno, K. Leong, O. K. Farha, M. Allendorf, R. P. Van Duyne and J. T. Hupp, *Chem. Rev.*, 2012, **112**, 1105.
16 Y. Zhao, H. Zeng, X. W. Zhu, W. Lu and D. Li, *Chem. Soc. Rev.*, 2021, **50**, 4484.
17 S. Hwang, W. S. Chi, S. J. Lee, S. H. Im, J. H. Kim and J. Kim, *J. Membr. Sci.*, 2015, **480**, 11.
18 C. Zhang, R. P. Lively, K. Zhang, J. R. Johnson, O. Karvan and W. J. Koros, *J. Phys. Chem. Lett.*, 2012, **3**, 2130.
19 H. T. Kwon and H.-K. Jeong, *J. Am. Chem. Soc.*, 2013, **135**, 10763.

20 K. Zhang, R. P. Lively, C. Zhang, R. R. Chance, W. J. Koros, D. S. Sholl and S. Nair, *J. Phys. Chem. Lett.*, 2013, **4**, 3618.
21 Z. Lai, *Curr. Opin. Chem. Eng.*, 2018, **20**, 78.
22 Y. Pan, Y. Liu, G. Zeng, L. Zhao and Z. Lai, *Chem. Commun.*, 2011, **47**, 2071.
23 J. H. Jo, C. O. Lee, G. Y. Ryu, H. Jae, D. Roh and W. S. Chi, *ACS Appl. Polym. Mater.*, 2022, **4**, 6426.
24 J. H. Jo, K. J. Kim, E. J. An, J. Lee, H. Jae, D. Roh and W. S. Chi, *ACS Appl. Mater. Interfaces*, 2024, **16**, 23799.
25 X. Wang, L. Wu, N. Li and Y. Fan, *J. Membr. Sci.*, 2021, **636**, 119582.
26 A. Knebel, A. Bavykina, S. J. Datta, L. Sundermann, L. Garzon-Tovar, Y. Lebedev, S. Durini, R. Ahmad, S. M. Kozlov, G. Shterk, M. Karunakaran, I. D. Carja, D. Simic, I. Weilert, M. Klüppel, U. Giese, L. Cavallo, M. Rueping, M. Eddaoudi, J. Caro and J. Gascon, *Nat. Mater.*, 2020, **19**, 1346.
27 C. Xin, Y. Ren, Z. Zhang, L. Liu, X. Wang and J. Yang, *ACS Omega*, 2021, **6**, 7739.
28 Y.-S. Bae, C. Y. Lee, K. C. Kim, O. K. Farha, P. Nickias, J. T. Hupp, S. T. Nguyen and R. Q. Snurr, *Angew. Chem., Int. Ed.*, 2012, **51**, 1857.
29 J. E. Bachman, Z. P. Smith, T. Li, T. Xu and J. R. Long, *Nat. Mater.*, 2016, **15**, 845.
30 B. L. Suh, T. Hyun, D. Y. Koh and J. Kim, *Chem. Mater.*, 2021, **33**, 7686.
31 H. Y. Cho, D. A. Yang, J. Kim, S. Y. Jeong and W. S. Ahn, *Catal. Today*, 2012, **185**, 35.
32 X. Wu, Z. Bao, B. Yuan, J. Wang, Y. Sun, H. Luo and S. Deng, *Microporous Mesoporous Mater.*, 2013, **180**, 114.
33 C. Chen, X. Feng, Q. Zhu, R. Dong, R. Yang, Y. Cheng and C. He, *Inorg. Chem.*, 2019, **58**, 2717.
34 J. Hu, Y. Chen, H. Zhang and Z. Chen, *J. Solid State Chem.*, 2021, **294**, 121853.
35 J. Hu, Y. Chen, H. Zhang, Z. Chen, Y. Ling, Y. Yang, X. Liu, Y. Jia and Y. Zhou, *Microporous Mesoporous Mater.*, 2021, **315**, 110900.
36 Z.-Y. Yao, J.-H. Guo, P. Wang, Y. Liu, F. Guo and W.-Y. Sun, *Mater. Lett.*, 2018, **223**, 174.
37 M. Díaz-García, Á. Mayoral, I. Díaz and M. Sánchez-Sánchez, *Cryst. Growth Des.*, 2014, **14**, 2479.
38 S. Lee, G. Lee and M. Oh, *Acc. Chem. Res.*, 2024, **57**, 3113.
39 C. Liu, J. Wang, J. Wan and C. Yu, *Coord. Chem. Rev.*, 2021, **432**, 213743.
40 J. Ha and H. R. Moon, *CrystEngComm*, 2021, **23**, 2337.
41 C. Liu, Q. Sun, L. Lin, J. Wang, C. Zhang, C. Xia, T. Bao, J. Wan, R. Huang, J. Zou and C. Yu, *Nat. Commun.*, 2020, **11**, 4971.
42 S. Li, L. Zhao, Y. Yao, Z. Gu, C. Liu, W. Hu, Y. Zhang, Q. Zhao and C. Yu, *CrystEngComm*, 2023, **25**, 284.
43 Y. Xu, X. Zhao, R. Chang, H. Qu, J. Xu and J. Ma, *J. Membr. Sci.*, 2022, **658**, 120737.
44 W. Hou, J. Cheng, N. Liu, C. Yang, Y. Chen, H. Zhang, B. Ye and J. Zhou, *J. Environ. Chem. Eng.*, 2022, **10**, 108029.
45 M. Abdollahzadeh, M. Chai, E. Hosseini, M. Zakertabrizi, M. Mohammad, H. Ahmadi, J. Hou, S. Lim, A. Habibnejad Korayem, V. Chen, M. Asadnia and A. Razmjou, *Adv. Mater.*, 2022, **34**, 2107878.
46 S. K. Gebremariam, A. M. Varghese, S. Kuppireddy, Y. Al Wahedi, A. AlHajaj, G. N. Karanikolos and L. F. Dumée, *Carbon Capture Sci. Technol.*, 2025, **14**, 100356.
47 Y. Wan, D. Kong, F. Xiong, T. Qiu, S. Gao, Q. Zhang, Y. Miao, M. Qin, S. Wu, Y. Wang, R. Zhong and R. Zou, *Chin. J. Chem. Eng.*, 2023, **61**, 82.
48 L. Liu, L. Chen, K. Thummavichai, Z. Ye, Y. Wang, T. Fujita and X. Wang, *Chem. Eng. J.*, 2023, **474**, 145858.
49 J. H. Jo, C. O. Lee, G. Y. Ryu, H. Jae, D. Roh and W. S. Chi, *ACS Appl. Polym. Mater.*, 2022, **4**, 6426.
50 Y. Wang, Y. Ren, H. Wu, X. Wu, H. Yang, L. Yang, X. Wang, Y. Wu, Y. Liu and Z. Jiang, *J. Membr. Sci.*, 2020, **602**, 117970.
51 B. Ghalei, K. Sakurai, Y. Kinoshita, K. Wakimoto, A. P. Isfahani, Q. Song, K. Doitomi, S. Furukawa, H. Hirao, H. Kusuda, S. Kitagawa and E. Sivaniah, *Nat. Energy*, 2017, **2**, 17086.
52 X. Guo, H. Huang, Y. Ban, Q. Yang, Y. Xiao, Y. Li, W. Yang and C. Zhong, *J. Membr. Sci.*, 2015, **478**, 130.
53 Y. Lee, C. Y. Chuah, J. Lee and T. H. Bae, *J. Membr. Sci.*, 2022, **647**, 120309.
54 K. J. Kim, Y. Gwon, E. J. An, J. Lee, J. H. Jo, S. Park and W. S. Chi, *Chemosphere*, 2024, **363**, 142926.
55 I. D. Carja, S. R. Tavares, O. Shekhah, A. Ozcan, R. Semino, V. S. Kale, M. Eddaoudi and G. Maurin, *ACS Appl. Mater. Interfaces*, 2021, **13**, 29041.
56 Y. Liu, W. Xie, S. Liang, X. Li, Y. Fan and S. Luo, *J. Membr. Sci.*, 2022, **646**, 120240.
57 N. Tien-Binh, H. Vinh-Thang, X. Y. Chen, D. Rodrigue and S. Kaliaguine, *J. Membr. Sci.*, 2016, **520**, 941.
58 X. Zhao, W. Liu, X. Liu and B. Zhang, *Ind. Eng. Chem. Res.*, 2021, **60**, 13927.
59 B. A. Habte, C. C. Hu, G. S. Liou, C. F. Wang, W. S. Hung, K. R. Lee and J. Y. Lai, *J. Membr. Sci.*, 2025, **735**, 124577.
60 B. Mirhosseini-Eshkevari, M. A. Ghasemzadeh, M. Esnaashari and S. T. Ganjali, *RSC Adv.*, 2021, **11**, 364.
61 M. T. Vu, R. Lin, H. Diao, Z. Zhu, S. K. Bhatia and S. Smart, *J. Membr. Sci.*, 2019, **587**, 117170.
62 M. Zunita, W. Natola O, M. David and G. Lugito, *Chem. Eng. J. Adv.*, 2022, **11**, 100320.
63 T. Zhao, C. Jia, H. Sun, R. Li, Z. Zhang, Y. Wang, J. Guo, F. Tian and C. Song, *Sep. Purif. Technol.*, 2026, **382**, 136067.
64 S. K. Gebremariam, A. M. Varghese, S. Kuppireddy, Y. Al Wahedi, A. AlHajaj, G. N. Karanikolos and L. F. Dumée, *Carbon Capture Sci. Technol.*, 2025, **14**, 100356.
65 J. Yang, F. Zhang, H. Lu, X. Hong, H. Jiang, Y. Wu and Y. Li, *Angew. Chem., Int. Ed.*, 2015, **54**, 10889.
66 J. Zhao, X. Quan, S. Chen, Y. Liu and H. Yu, *ACS Appl. Mater. Interfaces*, 2017, **9**, 28685.
67 Mansi, V. Shrivastav, P. Dubey, M. Hołdyński, S. Sundriyal, U. K. Tiwari and A. Deep, *Adv. Sustainable Syst.*, 2024, **8**, 2400043.
68 S. R. Hosseini, M. Omidkhah, Z. Mehri Lighvan, S. Norouzbahari and A. Ghadimi, *Sep. Purif. Technol.*, 2023, **307**, 122679.

69 Z. P. Gumus and M. Soylak, *Adv. Sample Prep.*, 2025, **13**, 100157.
70 W. Xu, D. R. Paul and W. J. Koros, *J. Membr. Sci.*, 2003, **219**, 89.
71 X. Bi, Y. Zhang, F. Zhang, S. Zhang, Z. Wang and J. Jin, *ACS Appl. Mater. Interfaces*, 2020, **12**, 49101.
72 Q. Zhao, Y. Sun, J. Zhang, F. Fan, T. Li, G. He and C. Ma, *J. Membr. Sci.*, 2024, **693**, 122326.
73 T. Rodenas, I. Luz, G. Prieto, B. Seoane, H. Miro, A. Corma, F. Kapteijn, F. X. Llabrés i Xamena and J. Gascon, *Nat. Mater.*, 2015, **14**, 48.
74 A. Jain, M. Z. Ahmad, A. Linkès, V. Martin-gil, R. Castro-muñoz, P. Izak, Z. Sofer, W. Hintz and V. Fila, *Nanomaterials*, 2021, **11**, 668.
75 C. T. Lee and M. W. Shin, *Surf. Interfaces*, 2021, **22**, 100845.
76 W. S. Chi, S. J. Kim, S.-J. Lee, Y.-S. Bae and J. H. Kim, *ChemSusChem*, 2015, **8**, 650.
77 C. Guo, J. Guo, Y. Zhang, D. Wang, L. Zhang, Y. Guo, W. Ma and J. Wang, *CrystEngComm*, 2018, **20**, 7659.
78 H. Irving and R. J. P. Williams, *J. Chem. Soc.*, 1953, 3192.
79 D. R. Lide, *CRC Handbook of Chemistry and Physics*, 86th edn, 2005.
80 W. Chen, Z. Huang, X. Liang, G. M. Kontogeorgis, B. Liu and G. Chen, *Fuel*, 2023, **331**, 125694.
81 X. Deng, L. Yang, H. Huang, Y. Yang, S. Feng, M. Zeng, Q. Li and D. Xu, *Small*, 2019, **15**, 1902287.
82 W. S. Chi, S. Hwang, S. J. Lee, S. Park, Y. S. Bae, D. Y. Ryu, J. H. Kim and J. Kim, *J. Membr. Sci.*, 2015, **495**, 479.
83 X. Han, T. Hu, Y. Wang, H. Chen, Y. Wang, R. Yao, X. Ma, J. Li and X. Li, *Sep. Purif. Technol.*, 2019, **214**, 61.
84 J. Cheng, C. Yang, W. Hou, N. Liu, R. Xia, Z. Chen, H. Zhang and J. Liu, *J. Membr. Sci.*, 2023, **670**, 121356.
85 Z. Gao, L. Liang, X. Zhang, P. Xu and J. Sun, *ACS Appl. Mater. Interfaces*, 2021, **13**, 61334.
86 R. P. Beiranvand and S. Ovaysi, *J. Chem.*, 2024, **2024**, 5944449.
87 Z. Guo, F. Yang, R. Yang, L. Sun, Y. Li and J. Xu, *Sep. Purif. Technol.*, 2021, **274**, 118949.
88 A. Mirandona-Olaeta, E. Goikolea, S. Lanceros-Mendez, A. Fidalgo-Marijuan and I. Ruiz de Larramendi, *Batteries*, 2023, **9**, 588.
89 L. Liao, X. Ding, J. Li, L. Huang, M. Zhang, Y. Fan, X. Zhou, Y. Zhang, S. Mo, Q. Xie and D. Ye, *Sep. Purif. Technol.*, 2023, **309**, 122939.
90 X. Gu, C. Huang, Z. Xu, H. Wu, R. Dong, R. Liu, J. Chen and H. Zhu, *J. Solid State Chem.*, 2021, **294**, 121803.
91 M. Díaz-García and M. Sánchez-Sánchez, *Microporous Mesoporous Mater.*, 2014, **190**, 248.
92 Y. G. Chung, E. Haldoupis, B. J. Bucior, M. Haranczyk, S. Lee, H. Zhang, K. D. Vogiatzis, M. Milisavljevic, S. Ling, J. S. Camp, B. Slater, J. I. Siepmann, D. S. Sholl and R. Q. Snurr, *J. Chem. Eng. Data*, 2019, **64**, 5985.
93 M. Rifqi Najib, N. Prasetyo and F. Inggit Pambudi, *Comput. Theor. Chem.*, 2024, **1238**, 114748.
94 A. Deacon, L. Briquet, M. Malankowska, F. Massingberd-Mundy, S. Rudić, T. l. Hyde, H. Cavaye, J. Coronas, S. Poulston and T. Johnson, *Commun. Chem.*, 2022, **5**, 18.
95 H. Shin, W. S. Chi, S. Bae, J. H. Kim and J. Kim, *J. Ind. Eng. Chem.*, 2017, **53**, 127.
96 R. Bardestani, G. S. Patience and S. Kaliaguine, *Can. J. Chem. Eng.*, 2019, **97**, 2781.
97 S. Li, W. Han, Q. F. An, K. T. Yong and M. J. Yin, *Adv. Funct. Mater.*, 2023, **33**, 2303447.
98 J. Ha, M. Jeon, J. Park, J. Kim and H. R. Moon, *Nanoscale Adv.*, 2023, **5**, 2111.
99 D. K. Panchariya, R. K. Rai, E. Anil Kumar and S. K. Singh, *ACS Omega*, 2018, **3**, 167.
100 D. I. Kolokolov, A. G. Stepanov and H. Jobic, *J. Phys. Chem. C*, 2015, **119**, 27512.
101 M. E. Casco, Y. Q. Cheng, L. L. Daemen, D. Fairen-Jimenez, E. V. Ramos-Fernández, A. J. Ramirez-Cuesta and J. Silvestre-Albero, *Chem. Commun.*, 2016, **52**, 3639.
102 F. Formalik, B. Mazur, M. Fischer, L. Firlej and B. Kuchta, *J. Phys. Chem. C*, 2021, **125**, 7999.
103 J. G. Flores, J. L. Obeso, V. Martínez-Jiménez, N. Martín-Guaregua, A. Islas-Jácome, E. González-Zamora, H. Serrano-Espejel, B. Mondragón-Rodríguez, C. Leyva, D. A. Solís-Casados, I. A. Ibarra, R. A. Peralta, J. Aguilar-Pliego and J. Antonio de los Reyes, *RSC Adv.*, 2023, **13**, 27174.
104 S. Ploychompoo, Q. Liang, X. Zhou, C. Wei and H. Luo, *Phys. E*, 2021, **125**, 114377.
105 S. Norouzbahari, Z. Mehri Lighvan, A. Ghadimi and B. Sadatnia, *Fuel*, 2023, **339**, 127463.
106 C. Shuai, X. Yuan, Y. Shuai, G. Qian, J. Yao, W. Xu, S. Peng and W. Yang, *Mater. Today Nano*, 2022, **18**, 100210.
107 K. Archana Yadav, G. Mishra, S. Kundu, S. Ghosh and R. Haldar, *Chem. Sci.*, 2025, **16**, 18161.
108 J. Peng, Z. Zhang, C. Hu, Z. Wang, Y. Kang, W. Chen and T. Ao, *J. Sol-Gel Sci. Technol.*, 2021, **99**, 339.
109 Q. Liu, X. Gao, Z. Liu, L. Gai, Y. Yue and H. Ma, *Materials*, 2023, **16**, 3378.
110 Z. Zhang, Y. Xiao, M. Cui, J. Tang, Z. Fei, Q. Liu, X. Chen and X. Qiao, *Dalton Trans.*, 2019, **48**, 14971.
111 J. A. Pereira de Figueiredo, M. J. Moreno Zapata, L. S. Amorim, J. A. de Oliveira Neto, D. R. Miquita, E. A. Soares, K. Balzuweit and C. B. Pinheiro, *ACS Omega*, 2024, **9**, 21939.
112 Y. Kim, T. Kim, J. Kim, N. Lee, S. H. Yoo, H. T. Kwon and K. Eum, *J. Membr. Sci.*, 2025, **723**, 123963.
113 Z. Song, F. Qiu, E. W. Zaia, Z. Wang, M. Kunz, J. Guo, M. Brady, B. Mi and J. J. Urban, *Nano Lett.*, 2017, **17**, 6752.
114 X. Liang, P. Wang, C. Li, M. Yuan, Q. Shi and J. Dong, *Microporous Mesoporous Mater.*, 2021, **320**, 111109.
115 W. Lou, J. Yang, L. Li and J. Li, *J. Solid State Chem.*, 2014, **213**, 224.
116 P. Karthik, R. Vinoth, P. Zhang, W. Choi, E. Balaraman and B. Neppolian, *ACS Appl. Energy Mater.*, 2018, **1**, 1913.
117 L. K. Njaramba, Y. Yoon and C. M. Park, *npj Clean Water*, 2024, **7**, 34.
118 M. W. Gaultois and A. P. Grosvenor, *J. Phys. Chem. C*, 2010, **114**, 19822.
119 J. Dechnik, C. J. Sumby and C. Janiak, *Cryst. Growth Des.*, 2017, **17**, 4467.

120 L. Zhang, Q. H. Zhu, Y. R. Zhou, S. L. Wang, J. Fu, J. Y. Liu, G. H. Zhang, L. Ma, G. Tao, G. H. Tao and L. He, *Nat. Commun.*, 2023, **14**, 8047.
121 R. Vakili, E. K. Gibson, S. Chansai, S. Xu, N. Al-Janabi, P. P. Wells, C. Hardacre, A. Walton and X. Fan, *ChemCatChem*, 2018, **10**, 4238.
122 R. A. Maia, B. Louis, W. Gao and Q. Wang, *React. Chem. Eng.*, 2021, **6**, 1118.
123 Z. Li, K. Shi, L. Zhai, Z. Wang, H. Wang, Y. Zhao and J. Wang, *Sep. Purif. Technol.*, 2023, **307**, 122725.
124 S. Nandi, R. Maity, D. Chakraborty, H. Ballav and R. Vaidhyanathan, *Inorg. Chem.*, 2018, **57**, 5267.
125 K. Akagi, H. Naito, T. Saikawa, M. Kotani and H. Yoshikawa, *Sci. Rep.*, 2024, **14**, 12021.
126 Z. Zhang, H. Zhu, H. Jin, Y. Cao, W. Fang, Z. Zhang, Q. Ma, J. Choi and Y. Li, *Angew. Chem., Int. Ed.*, 2025, **64**, e202415023.
127 H. M. Khalid, A. Mujahid, A. Ali, A. L. Khan, M. Saleem and R. M. Santos, *Int. J. Energy Res.*, 2024, **2024**, 2107340.
128 M. Z. Ahmad, T. A. Peters, N. M. Konnertz, T. Visser, C. Téllez, J. Coronas, V. Fila, W. M. de Vos and N. E. Benes, *Sep. Purif. Technol.*, 2020, **230**, 115858.
129 Y. Weng, W. Ji, C. Ye, H. Dong, Z. Gao, J. Li, C. Luo and X. Ma, *J. Membr. Sci.*, 2022, **644**, 120086.
130 D. Refaat, M. Yahia, H. D. Martínez-Hernández, M. Jimenez-Ruiz, V. Galván, V. Petrenko, R. Fernández de Luis and J. Coronas, *J. Mater. Chem. A*, 2025, **13**, 39254.
131 Z. X. Low, P. M. Budd, N. B. McKeown and D. A. Patterson, *Chem. Rev.*, 2018, **118**, 5871.
132 J. M. Hutchinson, *Prog. Polym. Sci.*, 1995, **20**, 703.
133 K. L. Gleason, Z. P. Smith, Q. Liu, D. R. Paul and B. D. Freeman, *J. Membr. Sci.*, 2015, **475**, 204.
134 A. M. W. Hillock and W. J. Koros, *Macromolecules*, 2007, **40**, 583.
135 F. Kadirkhan, P. S. Goh, A. F. Ismail, W. N. F. Wan Mustapa, M. H. M. Halim, W. K. Soh and S. Y. Yeo, *Membranes*, 2022, **12**, 71.
136 A. L. Ahmad, J. K. Adewole, C. P. Leo, S. Ismail, A. S. Sultan and S. O. Olatunji, *J. Membr. Sci.*, 2015, **480**, 39.